

# Effect of metal modification of titania and hydrogen co-feeding on the reaction pathways and catalytic stability in the acetone aldol condensation

Jorge Quesada, Laura Faba, Eva Díaz, and Salvador Ordóñez\*

Catalysis, Reactors and Control Research Group (CRC), Dep. of Chemical and Environmental Engineering, University of Oviedo, Oviedo 33006, Spain

\*Corresponding author

*E-mail address:* sordonez@uniovi.es (S. Ordóñez)

*Keywords:* catalytic deactivation, mesityl oxide, isophorones, methyl isobutyl ketone, bifunctional catalyst, C=C hydrogenation, platinum, nickel

## ABSTRACT

A stable performance of TiO<sub>2</sub> catalysts for gas-phase acetone aldol condensation was observed when reduced metals were added (Pt or Ni, 1.5 wt.%) and the reactions were conducted in presence of hydrogen. In both cases, the resulting metal-loaded catalysts are stable for 10 h, whereas continuous deactivation is observed for the parent TiO<sub>2</sub> catalyst (573 K). Both the activation of the H<sub>2</sub> molecule by metal nanoparticles and the change of the catalytic surface by metal insertion (in the case of Ni-loaded catalyst) enable suppressing oligomerization (by hindering enolates formation) and the strong adsorption of intermediates (by decreasing the concentration of high-strength acid-basic active sites), respectively.

More interestingly, these metals allow to tune the selectivity of the reaction. Indeed, the Ni-loaded titania catalyst is highly selective for the synthesis of  $\alpha,\beta$ -unsaturated ketones (selectivity to unsaturated C<sub>6</sub> and C<sub>9</sub> species >98 %, at ~12 % acetone conversion), whereas the Pt-loaded one is

highly selective to the formation of saturated C6 and C9 ketones (MIBK and DIBK, with selectivities >95 % at ~42 % acetone conversion).

The catalytic activity and stability of the two materials (Ni/TiO<sub>2</sub> and Pt/TiO<sub>2</sub>) in both absence and presence of H<sub>2</sub> are compared between them and with those of the parent TiO<sub>2</sub>. The results obtained by the reaction gas-phase analysis are supplemented through different solid characterization techniques (*i.e.*, CO<sub>2</sub>-TPD and NH<sub>3</sub>-TPD, HRTEM, XPS, TPO, and DRIFTS).

## 1. Introduction

Although large quantities of acetone are used all over the world (mostly in industrial processes as solvent or cleaning agent), its application as platform molecule to produce valuable commodities is also a very promising issue, attracting the attention of several researchers in recent years [1-4]. Its availability is ensured, being produced in huge amounts as byproduct in the synthesis of phenol by the cumene oxidation process [5]. In addition, several processes using biomass as raw material also produce acetone; such as the ABE (acetone-butanol-ethanol) fermentation or by biomass pyrolysis [6-9]. Therefore, using this acetone for the production of value-added chemicals with a traditional fossil origin (mesitylene, isobutene, etc.) brings an additional environmental incentive, related to the circular economy and the shift of the consumption of non-renewable resources [10,11].

The catalytic upgrading of acetone requires increasing its carbon-chain length. For this purpose, aldol condensation reaction is one of the most common alternatives [12]. In this light, the acetone self-condensation allows obtaining relevant chemicals such as mesityl oxide and isophorones (used in the manufacturing of paints, resins, adhesives, etc.) [13]. However, to the best of our knowledge, all the catalysts previously used for the production of unsaturated ketones from acetone show significant deactivation (*e.g.*, MgO, modified MgO, Mg-Zr mixed oxide, aluminosilicates, etc.) [2,4,14,15]. In fact, concerning the catalytic stability, the high-strength acid and basic active sites

favor strong adsorption of intermediates and formation of oligomers, respectively [4,13]. Based on this, tuning the surface chemistry of the catalyst in terms of both concentration and distribution of active sites should be considered for improving not only activity and selectivity, but also catalyst stability.

This stability might be also improved by performing the reaction in presence of molecular hydrogen together with a metallic phase that allows its activation by dissociative adsorption (bifunctional catalyst), what acid-basic materials cannot do. This enhancement could be brought by hindering the  $\alpha$ H abstraction of the ketone intermediates to form the enolates due to the presence of a significant surface concentration of hydrogen atoms. Consequently, this might imply a decrease of the aldol condensation ability of the catalytic system leading to downplaying, or even inhibiting, the oligomerization that ultimately results in strong adsorption and coke formation (*i.e.*, catalytic deactivation) [4]. On the other hand, this hypothesis could be concealed or suppressed because of the promotion of hydrogenation side-reactions as a consequence of the presence of both the molecular hydrogen and the metallic phase, which may fully or partially change the reaction pathways (depicted in **Scheme 1**). Furthermore, combining aldol condensation and hydrogenation reactions can yield saturated products, highlighting the methyl isobutyl ketone (MIBK) and diisobutyl ketone (DIBK) because of their relevant applications (*e.g.*, solvents, extracting agents, lubricants precursors, etc.) [16-19]. Typically, these compounds are co-produced from acetone, by a three-stage process [20,21], however merging aldol condensation and hydrogenation in an one-stage process by using a bifunctional catalyst presents relevant advantages.

In this work, two bifunctional anatase-TiO<sub>2</sub>-based catalysts (1.5 wt.% M/TiO<sub>2</sub>; M: Pt, Ni) were tested in the gas-phase acetone self-condensation with the aim of studying the effect of the presence of both the metallic active phase and the molecular hydrogen on the catalytic activity and stability. Thus, results obtained were compared with those reached when the parent TiO<sub>2</sub> was used, both in presence and in absence of molecular hydrogen. Both metals, platinum and nickel, were selected

since they are among the most active metallic phases to activate the hydrogen molecule [22,23]. The metal loading considered (*i.e.*, 1.5 wt.%) was low, trying to minimize the effects on the original-TiO<sub>2</sub> morphological properties and surface acidity-basicity (deeply analyzed by different characterization techniques). In addition to the analysis of the reaction gas-phase by gas chromatography, temperature programmed oxidation (TPO) and diffuse reflectance infrared Fourier transform spectroscopy (DRIFTS) were used to analyze the interaction of the reactant, products, and intermediates with the solid surface, allowing to obtain further insights on the deactivation processes.

## 2. Materials and methods

### 2.1. Catalyst synthesis

Parent anatase TiO<sub>2</sub> (Alfa Aesar, 99.6 %) was treated in flowing dry air (40 cm<sup>3</sup>·g<sup>-1</sup>·min<sup>-1</sup>) by heating up from 293 to 723 K at 10 K·min<sup>-1</sup>, holding the final temperature for 3 h, to ensure the stability of this material at reaction conditions. The Pt/TiO<sub>2</sub> catalyst was prepared from this pretreated TiO<sub>2</sub> by incipient wetness impregnation using a platinum precursor, Pt(NH<sub>3</sub>)<sub>4</sub>(NO<sub>3</sub>)<sub>2</sub> (Aldrich, 99.995 %). The aqueous solution of the precursor, 1.15 ml (5 wt.% Pt(NH<sub>3</sub>)<sub>4</sub>(NO<sub>3</sub>)<sub>2</sub>), was added dropwise (40 µl) on 2 g of pretreated TiO<sub>2</sub> in order to achieve 1.5 wt.% of platinum loading. The resulting material was dried at 383 K for 24 h before treating it, following the same procedure as the previously explained for the TiO<sub>2</sub> support. After this, the material was exposed to a 10 vol.% H<sub>2</sub>/Ar flow (100 cm<sup>3</sup>·g<sup>-1</sup>·min<sup>-1</sup>) and heated up from 298 to 673 K (5 K·min<sup>-1</sup>) holding the temperature for 1 h to ensure that all the metal is in its reduced state. This final temperature was chosen according to the the temperature-programmed reduction (TPR) results, shown in **Fig. S1** (Supplementary Material). Finally, the catalyst was cooled down to room temperature in flowing He (40 cm<sup>3</sup>·g<sup>-1</sup>·min<sup>-1</sup>). The 1.5 wt.% Ni/TiO<sub>2</sub> catalyst was synthesized following the same

procedure as the Pt/TiO<sub>2</sub>, using a 11.6 wt.% Ni(NO<sub>3</sub>)<sub>2</sub>·6H<sub>2</sub>O (Aldrich, 99.999 %) aqueous solution. After the catalysts preparation, both Pt/TiO<sub>2</sub> and Ni/TiO<sub>2</sub> as well as the treated parent TiO<sub>2</sub> were analyzed by different characterization techniques, being all the details included in the supplementary material (SM).

## 2.2. Reaction studies

Catalytic activity and stability experiments (duplicated; relative error < 3 %) were carried out at 573 K in a U-shaped fixed bed reactor (4.0 mm i.d.). The material sample (100 mg; 250-355 μm) was held by a quartz plug and kept at constant temperature using a PID-controlled furnace, and an internal thermocouple. The catalyst was pretreated at 673 K for 1 h before the catalytic experiment in flowing 20 vol.% H<sub>2</sub>/He (200 cm<sup>3</sup>·g<sup>-1</sup>·min<sup>-1</sup>) when testing bifunctional materials (Pt/TiO<sub>2</sub> and Ni/TiO<sub>2</sub>), but in He flow (200 cm<sup>3</sup>·g<sup>-1</sup>·min<sup>-1</sup>) in the case of parent TiO<sub>2</sub>. After this, the catalytic system was cooled down to the reaction temperature, keeping the gas stream. Acetone (0.017 cm<sup>3</sup>·min<sup>-1</sup>, VWR, ≥ 99.9%) was introduced into the gas flow (resulting in 20 mol%) by a liquid syringe-pump and vaporized in a heated transfer line (523 K), being 7.9 g<sub>ace</sub> · g<sub>cat</sub><sup>-1</sup> · h<sup>-1</sup> the weight hourly space velocity (WHSV). The reactor effluent stream was analyzed by gas chromatography (HP 6890Plus GC; TRB-5MS capillary column, 30 m, 0.25 mm) using a flame ionization detector (FID). Both retention times and response factors of the different compounds were determined by using standards. Additionally, the use of standards and speciation by mass spectrometry after gas-chromatographic separation (Shimadzu GCMS-QP2010), using the same column as in the GC-FID analyses and a similar temperature procedure, were used to complete the identification of the species.

## 2.3. Infrared analyses at reaction conditions

Infrared spectra were measured using DRIFTS in a Thermo Nicolet Nexus FT-IR equipped with the Smart Collector accessory and mercury cadmium telluride (MCT) detector. The material sample

(20 mg) was placed inside the temperature-controlled catalytic chamber. The catalyst was pretreated at 673 K for 1 h in flowing 20 vol. % H<sub>2</sub>/He (500 cm<sup>3</sup>·g<sup>-1</sup>·min<sup>-1</sup>) while analyzing the bifunctional materials, or in He flow (500 cm<sup>3</sup>·g<sup>-1</sup>·min<sup>-1</sup>) with the TiO<sub>2</sub>, before performing the experiment. The gas stream (500 cm<sup>3</sup>·g<sup>-1</sup>·min<sup>-1</sup> of He or 20 vol.% H<sub>2</sub>/He for inert or reducing atmosphere experiments, respectively) was saturated with acetone by passing through a bubbler at constant temperature (external cooling at *ca.* 273 K), before entering into the catalytic chamber. Signals were acquired in the 650 – 4000 cm<sup>-1</sup> wavenumber range, subtracting the KBr standard background. The Kubelka-Munk theory was used to convert the signals and to obtain the spectra, allowing semi-quantitative analyses and the comparison between different spectra.

### 3. Results and discussion

#### 3.1. Catalytic activity experiments in inert conditions

The presence of the metals causes slight changes on the morphological properties of the original surface of TiO<sub>2</sub>, observing a small decrease on specific surface area ( $S_{\text{BET}}$ ), pore size ( $d_p$ ), and pore volume ( $V_p$ ), as it is summarized in **Table 1**. These low differences are justified by the low metal loading. Accordingly, the results obtained by the X-ray diffraction (XRD) analyses show a clear anatase crystalline structure for both Pt/TiO<sub>2</sub> and Ni/TiO<sub>2</sub> (JCPDS 21-1272), without any peak related to either platinum or nickel metallic phases. The diffractograms are included in the SM, **Fig. S2**. However, the expected effect of supporting metal nanoparticles is related to the surface chemistry, which was analyzed by temperature programmed desorption of probe molecules (CO<sub>2</sub>-TPD and NH<sub>3</sub>-TPD). It must be pointed out that these TPD were carried out immediately after the reduction, preventing any contact with the atmosphere that could alter the reduced metal surface. These results are summarized in **Table 1**, being the corresponding profiles included in the SM (**Figs. S3 and S4**). In general, the concentrations of both basic and acid sites, especially medium and

strong ones, are reduced in the bifunctional materials, being this effect more relevant for the basic sites. Nevertheless, the most remarkable effect is related to the strength of these sites, with lower characteristic temperatures. This effect is mainly observed in the Ni/TiO<sub>2</sub>, with a notably decrease of medium and strong basic sites, shifting to weaker strength.

Preliminary catalytic studies were carried out in the acetone self-condensation without H<sub>2</sub> supplying to ascertain the catalytic behavior of each material. The aldol condensation is catalyzed by acid-basic pairs sites [13], hence the own presence of the metallic phase, in terms of catalytic activity, should not be of key significance. The evolution of the acetone aldol-condensation rate ( $r$ ) with the time-on-stream (TOS) for the three catalysts in the acetone self-condensation in absence of H<sub>2</sub> is shown in **Fig. 1**. At this point, it is worth to mention that these values are apparent rates in which not only consider the intrinsic kinetic but also the equilibrium, since they combine the effect of forward reactions (from ketones to  $\alpha,\beta$ -unsaturated ketones) and the reverse ones. The complexity of this mechanism prevents the easy estimation of each equilibrium constant independently. Acetone conversion values ( $x$ ) obtained at initial times, included in **Table 2**, are relatively low (highest conversion ~11 % with Ni/TiO<sub>2</sub>). Thus, differential reaction conditions can be considered, allowing kinetic analysis and comparison among catalysts in terms of reaction rates. The reaction rates experimentally obtained at initial times are 2.9, 2.7, and 4.1 mmol·g<sup>-1</sup>·ks<sup>-1</sup> with parent TiO<sub>2</sub>, Pt/TiO<sub>2</sub> and Ni/TiO<sub>2</sub>, respectively. According to the proposed model (detailed in section 3.3), the initial reaction rates at zero time on stream (line-fitting equation extrapolation, blue symbols in the Fig. 3) are 3.7, 2.7, and 6.3 mmol·g<sup>-1</sup>·ks<sup>-1</sup> with parent TiO<sub>2</sub>, Pt/TiO<sub>2</sub> and Ni/TiO<sub>2</sub>, respectively. The catalytic activity of parent TiO<sub>2</sub> and Pt/TiO<sub>2</sub> materials are very similar ( $r_{\text{Pt/TiO}_2}/r_{\text{TiO}_2} = 0.93$ ), whereas Ni/TiO<sub>2</sub> is more active ( $r_{\text{Ni/TiO}_2}/r_{\text{TiO}_2} = 1.41$ ). This result may be justified by the higher concentration of weak basic sites of Ni/TiO<sub>2</sub>, comparing to the rest of the catalysts. These weak sites seem to be strong enough to promote the acetone self-condensation but their weak character enhances the desorption rate of compounds obtained (C6 and C9), reducing

subsequent undesired oligomerizations and increasing the relative amount of free active sites to continue consuming acetone. A higher acetone conversion, then, is obtained at initial times. In good agreement with this hypothesis, Pt/TiO<sub>2</sub> and TiO<sub>2</sub> have similar concentration of weak basic sites, and lower than the Ni material. The slightly lower activity of Pt/TiO<sub>2</sub> regarding parent TiO<sub>2</sub> might be also explained by its lower concentration of acid sites, mainly the medium strength ones. The role of this sort of active sites in accomplishing both the dehydration step of the aldol condensation and stabilizing reaction intermediates has been previously pointed out in the literature [24].

Selectivities to the unsaturated C<sub>6</sub> (mesityl and isomesityl oxides) and unsaturated C<sub>9</sub> families (phorones, isophorones, and mesitylene) are included in **Fig. 2**, (being the values of initial and final measurements summarized in **Table 2**). The disaggregation of each family of compounds into the different components is detailed in the SM (**Table S1**). No other reaction product is identified apart from those mentioned above, hence the selectivities to C<sub>6</sub> and C<sub>9</sub> species are supplementary. Although the selectivity to C<sub>6</sub> and C<sub>9</sub> are similar at initial times with the three catalysts (~70 and ~30 % for C<sub>6</sub> and C<sub>9</sub>, respectively), their evolution with the TOS were slightly different. Thus, the selectivity to C<sub>9</sub> decreases more slowly when using TiO<sub>2</sub> than with the bifunctional materials, achieving values of zero around 29 ks of reaction time in contrast with 23 and 16 ks with the Pt/TiO<sub>2</sub> and Ni/TiO<sub>2</sub>, respectively. This different evolution of the selectivities suggests a detrimental effect of the presence of metals on the catalytic stability when operating in inert environment.

The parent TiO<sub>2</sub> is the most stable catalyst, but showing an activity drop of 93.5 % after 35 ks (**Fig. 1** and **Table 2**). Concerning both bifunctional materials, the activity decreases reached after the same TOS were 95.8 and 99.1 % with Pt/TiO<sub>2</sub> and Ni/TiO<sub>2</sub>, respectively. This higher activity drop with the bifunctional catalysts might be linked to their lower concentration of active sites, therefore the saturation of them by adsorbed intermediates occurs faster than in the case of the parent TiO<sub>2</sub>.

### 3.2. Catalyst performance in presence of H<sub>2</sub>

The same set of experiments as in the previous section were performed in presence of H<sub>2</sub> (20 vol.% H<sub>2</sub>/He). The evolution of the conversion with the TOS is shown in **Fig. 3** (initial and final values are included in **Table 2**), being the results obtained in absence of H<sub>2</sub> also included to make easier the comparison. As it was expected, the presence of hydrogen has a negligible effect on the activity of the parent TiO<sub>2</sub> (conversion decrease close to 6 % when H<sub>2</sub> was fed), since this material lacks metallic phase to activate the hydrogen molecule, not being able to perform other reactions different from the main one (aldol condensation). According to this, the gas-effluent analysis indicates the formation of the same chemical species as in inert conditions, without identifying new ones linked to hydrogenation reactions. The slightly lower conversion achieved when H<sub>2</sub> is supplied comparing with inert conditions could be linked to the non-dissociative adsorption of molecular hydrogen on the strong acid sites of TiO<sub>2</sub> (OH groups) [24,27], what would be in agreement with previous works which dealt with similar oxides (ZrO<sub>2</sub> and ZnO) [26]. This hypothesis has been checked by NH<sub>3</sub>-TPD of the catalytic surface once it was saturated with H<sub>2</sub>. Results are shown in the SM (**Fig. S5**). The original signal of the desorbed NH<sub>3</sub> detected at 690 K disappears when introducing the H<sub>2</sub>, suggesting the competitive adsorption of H<sub>2</sub> on these sites. In good agreement, the signal of H<sub>2</sub> shows a complex desorption pattern, suggesting different kinds of interactions with the catalyst surface. The blockage of part of the acid sites of the TiO<sub>2</sub> implies lower ability of this material to stabilize intermediates on its surface and to perform the dehydration step of the aldol condensation reaction, hence achieving lower acetone conversion rates. Nevertheless, differences in selectivity towards unsaturated C6 and C9 species working with the parent TiO<sub>2</sub> in presence of H<sub>2</sub> are very low (**Fig. 4** and **Table 2**), regarding those reached in inert conditions. Variations are noticed at initial times, at which the selectivity to unsaturated C9 was a bit higher in absence of H<sub>2</sub>, due to the slightly higher acetone conversion in comparison to the corresponding values obtained in presence of H<sub>2</sub>. Furthermore, the selectivity to unsaturated C9 never reaches zero values for the

TOS-range tested, unlike the results achieved in absence of H<sub>2</sub>, being in agreement with the lower deactivation observed in this experiment.

On the other hand, the presence of H<sub>2</sub> favors the improvement of the acetone conversion when working with both bifunctional catalysts, being worth to mention the high enhancement reached with the Pt/TiO<sub>2</sub> catalyst (improvements of 49 and 17 % with the Pt/TiO<sub>2</sub> and Ni/TiO<sub>2</sub>, respectively). In contrast with the results in inert conditions, the acetone conversion achieved with the bifunctional catalysts in presence of H<sub>2</sub> is kept almost constant (~42 and 12 % for Pt/TiO<sub>2</sub> and Ni/TiO<sub>2</sub>, respectively) for the whole experiment, as it can be noticed in **Fig. 3**.

The role of H<sub>2</sub> supplying not only affects the acetone conversion but also the selectivity distribution when working with Pt/TiO<sub>2</sub> (**Figs. 4 and 5**). Saturated C<sub>6</sub> and C<sub>9</sub> ketones (MIBK and DIBK, respectively) highlight as the main products, reaching selectivity values higher than 95 % (at ~42 % of acetone conversion), being better results than those reported in the literature [27-30]. Furthermore, the selectivity towards MIBK is kept almost constant for all the reaction time (63.7 %), with only a little drop of 6.5 % of the initial value after 36 ks. This decrease was directly linked to an increase of the selectivity to DIBK, which is kept around values of 31.5 %. Further hydrogenation, C=O functional group, is almost discarded since only traces of methyl isobutyl carbinol (MIBC) are identified, confirming the selective C=C bond hydrogenation by platinum.

Additionally, traces of 2-propanol (obtained by acetone hydrogenation) are also detected, which is in agreement with the fast acetone aldolization step observed on alike acid-basic materials at similar temperatures [13]. Low amounts of unsaturated C<sub>6</sub> and C<sub>9</sub> compounds (those detected in inert conditions) are determined, achieving selectivities of only 1.0 and 2.6 %, respectively. The remaining compounds produced are acetic acid, and a mix of isobutene and isobutane (obtained by isobutene hydrogenation) formed from C<sub>6</sub> by radical-mediated pathways [31]. These species are not detected in absence of H<sub>2</sub> due to the lower conversion achieved. In this light, taking into account

that the acetone aldol condensation is a reversible reaction [13], and subsequent aldol condensations and hydrogenations are closely interrelated, the high promotion of hydrogenations (*i.e.*, formation of saturated higher-ketones) pushes previous steps, justifying the enhancement of the acetone conversion rate noticed with this catalytic system in presence of H<sub>2</sub>.

Concerning the Ni/TiO<sub>2</sub> catalyst in presence of H<sub>2</sub>, almost no saturated products are formed during reaction, with only small selectivities to MIBK (1.2 %), although no deactivation is observed (constant conversion ~12 %). Therefore, the formation of saturated higher-ketones is not favored with this catalyst, implying a bit higher acetone conversion as that reached in inert conditions, in contrast with the Pt/TiO<sub>2</sub>. On the other hand, it is suggested that the H<sub>2</sub> supplying in presence of nickel nanoparticles hinders the  $\alpha$ H abstraction of higher-ketones ( $\geq$  C<sub>9</sub>) to form their respective enolates, reducing the aldol condensation capacity of this catalytic system (minimizing or eliminating the oligomerization and coke formation). This hypothesis is based on the disturbance effect of dissociated hydrogen atoms adsorbed on the support (moved by spillover) that prevents subsequent aldolizations of C<sub>9</sub> compounds. This discussion is illustrated in **Fig. S6**. This fact also entails keeping the conversion almost constant; and obtaining significant unsaturated C<sub>9</sub> selectivities during the experiment, whereas in absence of H<sub>2</sub>, the formation of this fraction is suppressed after 16 ks on stream. Thus, the mean values of the selectivity to unsaturated C<sub>6</sub> and C<sub>9</sub> are 62.6 and 35.9 %, respectively. In good agreement with the low hydrogenation capacity and low conversion, only traces of 2-propanol were detected, and neither acetic acid nor isobutene formation is noticed.

The results obtained using the bifunctional catalysts are rather different between them when operating in reducing conditions. Considering that the spillover phenomenon must occur in a similar extent with both bifunctional materials, the significantly higher reducing activity observed with Pt/TiO<sub>2</sub> is assumed to be due to a higher activity of this metal for the selective C=C hydrogenation than nickel [23]. This hypothesis implies a hydrogenation strongly conditioned by the metal activity,

and an almost null effect of spillover. According to the literature [28,32,33], it is presumed that the Ni/TiO<sub>2</sub> should accomplish satisfactory results in terms of both MIBK and DIBK selectivities. However, experimental results reject this hypothesis. In order to gain knowledge about this unforeseen behavior of the Ni/TiO<sub>2</sub> and to explain the discrepancies noticed when comparing it with the Pt/TiO<sub>2</sub>, both catalysts were analyzed in depth by different characterization techniques.

The metal dispersion ( $D$ ) seems to be the key parameter, since the dissociative adsorption of H<sub>2</sub> is produced by the metal atoms of the nanoparticles that are exposed to the reaction environment. Thus, the principal hypothesis of the low hydrogenation capacity of the Ni/TiO<sub>2</sub> could be associated with a very low metal surface area. Based on this, the bifunctional catalysts and the bare TiO<sub>2</sub> were analyzed by high-resolution transmission electron microscopy (HRTEM). As expected, the parent TiO<sub>2</sub> consists of anatase (**Fig. S7**), confirmed by the d-spacing of the (011) plane of this crystalline phase (*i.e.*, 3.52 Å). Platinum nanoparticles of 1.6 nm of mean particle size ( $d_m$ ), corresponding to  $D = 70\%$ , are supported on the TiO<sub>2</sub>, as shown in **Fig. 6a**. Nevertheless, the presence of nanoparticles concerning the Ni/TiO<sub>2</sub> is not as clear as in the case of the Pt/TiO<sub>2</sub>, since no other crystalline phase different from anatase is easily noticeable (**Fig. 6b**). Some nickel nanoparticles were found when increase the magnification and comparing the d-spacing values determined with those of the nickel metallic crystalline phase (JCPDS 45-1027). One of the nickel nanoparticles is shown in **Fig. 7a**, the d-spacing measured (2.03 Å) is resembling to that corresponding to the (011) plane of metallic nickel (2.01 Å). According to the TPR results (**Fig. S1**), a broad particle size distribution can be assumed in the case of Ni/TiO<sub>2</sub>, in contrast to Pt/TiO<sub>2</sub>, whose narrow peak denote a very controlled particle size. It can be noted that the contrast is much poorer than that observed in the Pt/TiO<sub>2</sub> micrographs due to closer atomic number between titanium and nickel with regard to titanium and platinum. Based on this, only the biggest particles can be easily identified. Taking into account that the metal loading is the same for both materials (1.5 wt.%) but the nanoparticles of the Ni/TiO<sub>2</sub> are much larger (higher than 10 nm according to micrograph shown in **Fig. 7a**), the amount

of nickel particles per unity of surface area of the TiO<sub>2</sub> support is lower. This fact might condition its activity since the average distance between the metal nanoparticles and the acid-basic active sites of the TiO<sub>2</sub> support could be too high to favor the cascade reactions needed. Furthermore, a different crystalline phase (d-spacing of 2.81 Å) is formed as a thin layer on part of the anatase structure, as it can be observed in **Fig. 7b**. This crystalline phase does not correspond to any of the NiO (alpha and beta; JCPDS 44-1159 and 4-835, respectively). Therefore, this suggests that: (i) crystallites of a new structure are created by insertion of nickel atoms into the original anatase TiO<sub>2</sub> phase during the thermal treatment at high temperature (see catalyst synthesis, section 2.1); and (ii) nickel nanoparticles are in metallic state, in good agreement with TPR results (**Fig. S1**), hence ruling out their incomplete reduction as the low hydrogenation-activity cause.

The hypothesis of the formation of nickel-inserted crystallites during the thermal treatment suggests an interfacial phenomenon for which the nickel atoms would not be introduced into the support bulk but into its surface. Due to this, X-ray photoelectron spectroscopy (XPS) experiments were performed to check whether nickel was partially coordinated by the analysis of its oxidation state. **Fig. 8a** shows the nickel 2p region obtained through XPS analysis. Although the signal has a lot of noise, interesting events can be noticed. The binding energy signal splits into two areas corresponding to the 2p doublets (2p<sub>3/2</sub>: 851 – 859 eV; and 2p<sub>1/2</sub>: 869 – 876 eV). The main peak, 2p<sub>3/2</sub> doublet, is associated with Ni<sup>2+</sup> (854 – 857 eV). Moreover, peak broadening towards lower binding energy related to Ni<sup>0</sup> is also noted (852 – 854 eV) [34]. Within the region concerning the 2p<sub>1/2</sub> doublet, the main peak linked to Ni<sup>2+</sup> arises at 873 eV, whereas a lower one at 870 eV corresponding to Ni<sup>0</sup> is also observed (slight increase of the spectrum at this binding energy in **Fig. 8a**) [35]. Furthermore, another peak appears at 861.8 eV, being a shake-up satellite of the Ni<sup>2+</sup> 2p<sub>3/2</sub> peak [36]. As a result, it can be concluded that the nickel is mainly in its Ni<sup>2+</sup> oxidation state while a lower amount is in the Ni<sup>0</sup> one (Ni<sup>0</sup>/Ni<sup>2+</sup> XPS 2p<sub>3/2</sub> area ratio of 0.5). Concerning the titanium 2p region, two peaks corresponding to binding energies of 459.7 and 465.4 eV linked to the 2p<sub>3/2</sub>

and  $2p_{1/2}$  doublets, respectively [37], can be observed for the parent  $\text{TiO}_2$  (**Fig. 9a**). However, the spectrum obtained for this region in the case of the  $\text{Ni/TiO}_2$  is partially different (**Fig. 9b**). Despite the fact that the same peaks as for the original  $\text{TiO}_2$  are present (459.2 and 464.8 eV), a new pair of peaks at binding energies of 457.3 and 462.9 eV arise. The former peak could match with the titanium  $2p_{3/2}$  signal of titanium-nickel mixed oxide [38], and therefore it is suggested that the latter one might correspond to its respective  $2p_{1/2}$  doublet. Consequently, this supports the hypothesis of the formation of crystallites of titanium-nickel mixed oxides on the anatase  $\text{TiO}_2$  surface. In addition, in spite of the nickel loading, the negligible shift of the binding energies of the  $\text{TiO}_2$  peaks (what would be produced by interaction of  $\text{TiO}_2$  with nickel) confirms the low amount and poor distribution of the nickel nanoparticles on the  $\text{TiO}_2$  surface.

The insertion of nickel atoms in the anatase  $\text{TiO}_2$  structure to form a new crystalline phase might be related to the high decrease of the medium and strong basic sites of the resulting  $\text{Ni/TiO}_2$  material (*vide supra*; see section 3.1). Indeed, this sort of active sites corresponds to low coordinated oxygen atoms (isolated  $\text{O}^{2-}$ ) [24]. These electron-rich atoms could interact during the thermal treatment with the  $\text{Ni}^{2+}$  cations deposited on them, leading to coordination between  $\text{Ni}^{2+}$  and that  $\text{O}^{2-}$  species of the anatase lattice which ultimately creates the new crystalline structure observed. This assumption also justifies the shift of the medium and strong basic active sites to weak strength ones when increasing the coordination of the isolated oxygen atoms.

To sum up, it is proposed that both the unsuitable surface distribution of nickel nanoparticles to accomplish hydrogenation reactions and the almost negligible concentration of mainly strong basic active sites (which implies low capacity of oligomerization by subsequent aldol condensation reactions) may lead to synergistic effects on the acetone self-condensation in presence of  $\text{H}_2$ , inhibiting the catalyst deactivation but keeping almost the same activity as working in inert conditions (in terms of both acetone conversion and product selectivities). In this light,  $\text{Ni/TiO}_2$  and

reducing conditions are proposed for the stable formation of unsaturated ketones (mainly mesityl oxide and isophorones).

XPS analyses were also performed for the Pt/TiO<sub>2</sub> catalyst (**Fig. 8b**). Due to the presence of aluminum in the original TiO<sub>2</sub> (0.01 wt.% as defined in the certificate of analysis provided by the manufacturer), the analysis was focused on the platinum 4d region, instead of the common utilized 4f one, to avoid the interference with the aluminum 2p region characterized by similar binding energies of approximately 74 eV [39,40]. The binding energy signal consists of two differentiated areas corresponding to the 4d doublet pairs (4d<sub>5/2</sub> and 4d<sub>3/2</sub>). Both peaks observed at 313.9 and 330.9 eV are related to the 4d<sub>5/2</sub> and 4d<sub>3/2</sub> doublets of Pt<sup>0</sup> [41]. In addition, an almost negligible peak associated to Pt<sup>4+</sup> arises at 317.8 eV [42]. As a consequence, it is confirmed that the platinum is present as Pt<sup>0</sup> oxidation state as nanoparticles (Pt<sup>0</sup>/Pt<sup>4+</sup> XPS 4d<sub>5/2</sub> area ratio of 16.4), in agreement with its easy reducibility after thermal treatment even at low temperature [43]. Furthermore, no mixed-oxides crystallites of titanium and platinum are formed comparing the nickel material. This fact could be explained by two reasons: (i) as a noble metal, platinum is hardly involved in mixed structures with other metals; and (ii) platinum atoms are much larger than the titanium ones, hence hindering their insertion into the TiO<sub>2</sub> to generate a new hybrid phase.

Regarding the titanium 2p region of the Pt/TiO<sub>2</sub> XPS analysis (**Fig. 9c**), in contrast to the Ni/TiO<sub>2</sub>, the same peaks as for the parent TiO<sub>2</sub> are noticed, otherwise they arise at lower binding energies (457.7 and 463.4 eV). This last fact is proposed to be directly related to the presence of the well-distributed platinum nanoparticles on the TiO<sub>2</sub>. However, it can be assumed that the peak at lower binding energy (*i.e.*, 2p<sub>3/2</sub> doublet) is formed by the contribution of two overlapping peaks (456.9 and 458.2 eV), suggesting that unlike titanium species in terms of coordination exist on the surface. This would be caused by the dissimilar degree of interaction of the titanium atoms with the platinum nanoparticles (interface and non-interface titanium atoms).

Hydrogen chemisorption analyses of both Pt/TiO<sub>2</sub> and Ni/TiO<sub>2</sub> are in line with the results previously observed by other techniques. The H<sub>2</sub> uptake per metal atom is two orders of magnitude lower in the case of the Ni/TiO<sub>2</sub> ( $7.41 \cdot 10^{-29}$  and  $7.83 \cdot 10^{-27}$  m<sup>3</sup> H<sub>2</sub>·atom<sup>-1</sup>, for Ni/TiO<sub>2</sub> and Pt/TiO<sub>2</sub>, respectively), therefore confirming its lower active metallic surface ( $1.33$  and  $51.96$  m<sup>2</sup>·g<sub>metal</sub><sup>-1</sup>, for Ni/TiO<sub>2</sub> and Pt/TiO<sub>2</sub>, respectively). Accordingly, the calculations obtained in terms of mean particle size and metal dispersion cannot be considered since, as it was observed, not all the nickel atoms are taking part in metallic nanoparticles. However, the mean particle size and metal dispersion determined for the Pt/TiO<sub>2</sub> (1.5 nm and 75 %, respectively) are very similar to those ascertained by HRTEM (1.6 nm and 70 %, respectively). Furthermore, another interesting difference between both bifunctional catalysts is noticed by doing a second hydrogen chemisorption cycle. Whereas the capacity of Pt/TiO<sub>2</sub> to chemisorb hydrogen seems to be kept in the second cycle with only 3 % of loss ( $7.58 \cdot 10^{-27}$  Nm<sup>3</sup> H<sub>2</sub>·atom<sup>-1</sup>), the chemisorbed hydrogen is reduced in 20 % in the case of the Ni/TiO<sub>2</sub> ( $5.91 \cdot 10^{-29}$  Nm<sup>3</sup> H<sub>2</sub>·atom<sup>-1</sup>). This drop of the capacity to chemisorb hydrogen at room temperature (308 K in this case) in subsequent analysis cycles is closely associated with a phenomenon known as Strong Metal-Support Interaction (SMSI) [44]. As it was reported [44], the SMSI is quite common for metal-supported titania catalysts and, mainly, considered as simple site blocking when nickel as metal, but being able to contribute to lower catalytic activity.

### 3.3. Analysis of the catalytic stability

In order to model and evaluate the catalyst deactivation operating in both presence and absence of H<sub>2</sub>, a power-law deactivation kinetics was considered (**eq. 1**) [45]:

$$r_d = -da/dt = k_d \cdot C_A^\alpha \cdot a^d \quad (1)$$

where  $r_d$  is the deactivation rate,  $a$  is the catalyst activity,  $t$  is the time-on-stream (TOS),  $d$  is the deactivation rate order,  $k_d$  is the deactivation rate constant, and  $\alpha$  is the exponent that specifies the dependence of the deactivation rate on the acetone concentration ( $C_A$ ) affecting deactivation.

Considering: (i) first-order deactivation kinetics ( $d = 1$ ); (ii) the independence of the deactivation rate on the  $C_A$  ( $\alpha = 0$ ) because of the differential conditions of operation ( $C_A$  almost constant with the reaction time); and (iii) the relation between the acetone reaction rate ( $r$ ) and the catalyst activity (**eq. 2**), the acetone reaction rate can be described as follows (**eq. 3**):

$$r = r_0 \cdot a \quad (2)$$

$$r = r_0 \cdot \exp(-k_d \cdot t) \quad (3)$$

being  $r_0$  the acetone reaction rate at zero time. Furthermore, the evolution of the acetone conversion can be depicted in terms of the deactivation rate constant (**eq. 4**), taking into account the relation between the reaction rate and conversion through the space velocity ( $SV$ ) (**eq. 5**):

$$x = x_0 \cdot \exp(-k_d \cdot t) \quad (4)$$

$$r = SV \cdot x \quad (5)$$

where  $x_0$  is the acetone conversion at zero time.

The calculated  $k_d$  values are included in **Fig. 3**. Regarding the catalytic stability of the parent  $\text{TiO}_2$  in presence of  $\text{H}_2$ , the  $k_d$  ( $0.058 \text{ ks}^{-1}$ ) decreases in 32 % comparing to the value obtained in absence of  $\text{H}_2$  ( $0.086 \text{ ks}^{-1}$ ). This improvement might be related to the worse molecule-stabilization capacity of this material because of the  $\text{H}_2$  presence, as explained above, which hinders the strong adsorption of oligomers and coke formation on the catalytic surface resulting in softer deactivation. Although differential reaction conditions cannot be considered in this case when using  $\text{Pt/TiO}_2$  (high acetone conversion), the  $k_d$  are determined in inert conditions ( $0.096 \text{ ks}^{-1}$ ) and in the reducing ones ( $2.5 \cdot 10^{-4} \text{ ks}^{-1}$ ). In the last case, value obtained is lower than the threshold deemed by Herrmann and Iglesia (no deactivation when  $k_d < 0.05 \text{ ks}^{-1}$ ) [11].

The analysis in the case of  $\text{Ni/TiO}_2$  is more complex, because of the co-presence of more than one deactivation causes. Concerning the faster deactivation observed with the  $\text{Ni/TiO}_2$  comparing

with parent TiO<sub>2</sub> in inert conditions, it would be due to the Ni<sup>2+</sup> sites (resulting from Ni insertion on the TiO<sub>2</sub> surface) that act as Lewis acid sites but with lower strength than the corresponding Ti sites that they are replacing. Following this line, the acid-basic pairs in which Ni<sup>2+</sup> takes part show lower ability to favor the dehydration of the aldol by the E<sub>2</sub> mechanism (**Fig. S8**; step (iii) and (iv)), promoting the stable adsorption of aldol intermediates. This phenomenon must be added to the common deactivation process of the acid-basic surfaces (TiO<sub>2</sub>, in this case) in this type of reaction because of subsequent aldol condensation and oligomerization. Due to the low proportion of Ni<sup>2+</sup> sites, the former contribution only affects deactivation at low TOS. In fact, the assumption of these two deactivation mechanisms in the case of the Ni/TiO<sub>2</sub> in absence of H<sub>2</sub> is confirmed by the lines of fit for the acetone reaction rate with the time-on-stream (**Fig. 3**). It can be noticed that below 20 ks the overall deactivation would be due to the combination of the two mechanisms proposed. However, over 20 ks, it seems that all the Ni<sup>2+</sup> sites are deactivated, and therefore only the stable adsorption on TiO<sub>2</sub> support is the responsible of the deactivation. In fact, the deactivation rate constant ( $k_d$ ) above 20 ks can be considered the same than that corresponding to parent TiO<sub>2</sub> in inert conditions (0.085 and 0.086 ks<sup>-1</sup>, respectively). The experimental confirmation of these hypotheses requires a deep analysis of the evolution of solid surface at reaction conditions.

TPO and DRIFTS experiments were realized with the aim of completing the gas-phase assessment by analyzing the solid-phase (*i.e.*, the chemical species adsorbed on the catalyst surface and the nature of that interaction). The TPO analyses were carried out with the catalyst used-samples recovered after 36 ks of TOS in absence and presence of H<sub>2</sub> (**Fig. 10**). The allocation of the combustion temperature frames of the different species (*i.e.*, C6, C9, and heavier compounds) is explained in the SM. The TPO profiles obtained with the parent TiO<sub>2</sub> show the presence of heavy compounds, mainly C9 species, on the catalytic surface regardless of the reaction conditions. These results are in agreement with the gas-phase analysis. Moreover, the hypothesis suggested of selective acid-site blockage by molecular hydrogen is confirmed, since the saturation degree of the

surface is lower when H<sub>2</sub> is fed, in spite of observing the same adsorbed species. The TPO analyses with both bifunctional materials show, not only much lower degree of saturation of the surface when H<sub>2</sub> is supplied (like working with the parent TiO<sub>2</sub>), but also the characteristic combustion-temperature of the species adsorbed are quite different (unlike the results obtained with the parent TiO<sub>2</sub>). Thus, the presence of C<sub>9</sub> species on the surface of both materials disappear when working with H<sub>2</sub> and, particularly, there are almost no compounds adsorbed on the Pt/TiO<sub>2</sub>. This fact confirms that the presence of H<sub>2</sub> together with metallic phase have a significant role in the reaction. On this basis, it is considered that the catalytic surface hold the hydrogen atoms produced on the metallic nanoparticles as adatoms, which can move on the surface by spillover [44]. As introduced above (see catalytic activity experiments, section 3.2), these hydrogen adatoms stabilize different intermediates from those favored working in inert conditions, which may imply: (i) the formation of saturated compounds by hydrogenation reactions (ketones and alcohols, by C=C and C=O hydrogenation, respectively) in the case of the Pt/TiO<sub>2</sub>; and/or (ii) the decrease of the aldol condensation capacity by hindering enolates formation (key step of the aldol condensation reaction). The second effect, with a significant lower weight in the product distribution, is the only one observed in the case of the Ni/TiO<sub>2</sub> because of the negligibility of the first one. As a result, subsequent oligomerization, strong adsorption of intermediates and, ultimately, coke formation are extensively hampered, or even suppressed, inhibiting deactivation.

DRIFTS experiments were carried out at different reaction time in presence and absence of H<sub>2</sub>. The main interesting regions of spectra obtained with the three catalysts in reducing conditions are shown in **Fig. 11** (the complete spectra recorded with Pt/TiO<sub>2</sub> and Ni/TiO<sub>2</sub>, are included in the SM, **Figs. S9** and **S10**). Analogous spectra in inert conditions are included in the SM (**Fig. S11**). These results are not included in the main manuscript since the most interesting information is analyzed as function of the evolution of spectra in reducing conditions. Taking into account the semi-quantitative character of Kubelka-Munk analysis, key conclusions are related to the comparison

between different spectra. This premise allows multiplying each of the three main interesting regions by a different factor, with the only aim of make easier the comparison.

In general terms, same bands are identified in all the spectra, both in inert or reducing environment. This is due to the presence of identical functional groups in almost each adsorbed molecule (*i.e.*, reactant, intermediates, and products) irrespective of the operating conditions. Although this fact makes the spectra analysis difficult in terms of distinguishing between unlike adsorbed species, some interesting differences can be pinpointed especially with reference to the saturation degree of the infrared bands observed. The band at  $1740\text{ cm}^{-1}$ , related to the C=O stretching vibration mode of ketones [46,47], is the most significant regardless the material used. Other important bands are observed at  $1220$  and  $1350\text{ cm}^{-1}$ , associated with stretching vibration modes of C-C and bending C-(CH<sub>3</sub>)<sub>2</sub>, respectively [46,48]. Another common band between all materials is noticed around  $3000\text{ cm}^{-1}$ , due to stretching vibration modes of C-H, C-H<sub>2</sub>, and C-H<sub>3</sub> [49]. Consequently, this band is strongly related to long carbon-chain species. Two additional bands at  $1440$  and  $1580\text{ cm}^{-1}$  are almost only observed with the parent TiO<sub>2</sub> catalyst, linked to the C-(CH<sub>3</sub>)<sub>2</sub> stretching vibration mode of mesitylene and stretching of the C=C bond [46,49].

Concerning the spectra in inert conditions, no relevant differences are observed, being not only the peaks but also the intensities almost constant, despite the material or the TOS. This fact suggests that deposition phenomena occur in almost the same extent in all the cases, in good agreement with the similar concentration of strong acid sites (active sites typically related to the strong deposition of unsaturated carbon molecules [49-51]). Considering the proximity of the entire base and acid sites (acid-base pairs), this deposition can block part of the basic sites, active for the main reaction. The lower concentration of these sites, the higher relevance of this effect, being more noticeable in the case of Ni/TiO<sub>2</sub>. Furthermore, in the specific case of Ni/TiO<sub>2</sub>, the deactivation of Ni<sup>2+</sup> acid sites previously proposed by the deactivation model is confirmed by the presence of the band at  $3400\text{ cm}^{-1}$

<sup>1</sup> linked to the O-H stretching mode [52]. This vibration mode could correspond to adsorbed water or the alcohol group of aldol intermediates (**Fig. S12**).

The main conclusion of comparing spectra in inert and reducing atmosphere is the lower intensity of all the signals detected with bifunctional catalysts (even observing the same bands) in the experiments performed in reducing conditions. This expected behavior is in good agreement with the lower concentration of unsaturated molecules and the lower affinity between the saturated ones and the catalytic surface (observed in the TPO experiments). This lower adsorption, clearly observed in the evolution of the gas phase, is directly related to the observed improved stability. Thus, the spectra of Pt/TiO<sub>2</sub> and Ni/TiO<sub>2</sub> kept constant the intensities during the reaction, whereas they slightly increased with the parent TiO<sub>2</sub> below 28.8 ks and highly raised over this reaction time, suggesting higher strong adsorption of the intermediates formed (**Fig. 11a**). This fact is in agreement with the results obtained from the catalytic stability and TPO experiments, since no stability loss were observed in presence of H<sub>2</sub> with the bifunctional materials in contrast with the parent TiO<sub>2</sub>. Comparing the Pt/TiO<sub>2</sub> and the Ni/TiO<sub>2</sub> spectra (**Figs. S9 and S10**), no differences can be observed except for the band related to stretching C-H, C-H<sub>2</sub>, and C-H<sub>3</sub> that is slightly high in intensity with the Ni/TiO<sub>2</sub> (**Fig. 11b**). This event would be due to the formation of C<sub>6</sub> species in a greater extent with this material, as it was previously noticed by the TPO analyses.

#### 4. Conclusions

The hypothesis of improving the catalytic stability in the gas-phase acetone self-condensation by operating in presence of H<sub>2</sub> has been successfully checked by combining continuous-flow reactions and deep characterization of fresh and spent catalysts. The stability of the parent TiO<sub>2</sub> is enhanced due to the blockage of the strong acid sites by non-dissociative adsorption of H<sub>2</sub> (drop of 32 % in the deactivation kinetic constant). However, this effect is much more remarkable with the

bifunctional materials (Pt/TiO<sub>2</sub> and Ni/TiO<sub>2</sub>), without catalytic deactivation during all the TOS tested (10 h), since they own metal nanoparticles that activate the H<sub>2</sub> supplied. Changes because of the H<sub>2</sub> feeding also affect the product distribution and initial conversion, observing two different situations. On one hand, the activity of Pt/TiO<sub>2</sub> is clearly improved (~42 % of acetone conversion; from a 7.1 % in inert conditions) being this enhancement justified by the almost complete C=C hydrogenation of the acetone aldol condensation intermediates, obtaining saturated C<sub>6</sub> and C<sub>9</sub> ketones as main products (lumped selectivity to MIBK and DIBK >95 %).

On the other hand, the Ni/TiO<sub>2</sub> catalyst does not show any significant hydrogenation capacity, yielding unsaturated C<sub>6</sub> and C<sub>9</sub> compounds (lumped selectivity >98 %; ~12 % of acetone conversion). This unprecedented behavior is explained as a consequence of two synergistic effects: (i) the poor distribution of Ni nanoparticles in the support; and (ii) the modification of the surface chemistry in terms of basicity by the insertion of nickel atoms into the TiO<sub>2</sub> structure (decrease of strong basic sites). Thus, the results obtained in this work can be considered as a starting point for the development of high-performing stable catalysts for the production of  $\alpha,\beta$ -unsaturated ketones from acetone.

## **Acknowledgments**

This research project was supported by the Ministry of Science, Innovation and Universities of the Government of Spain (CTQ2017-89443-C3-2-R) and the Regional Government of the Principality of Asturias (IDI/2018/000116).

## **Appendix A. Supplementary material**

Supplementary data to this article can be found online at: <https://doi.org/10.1016/j.jcat>.

Details of the catalyst characterization techniques ( $N_2$ -physisorption, TPR, TPD, XRD, HRTEM, XPS,  $H_2$ -chemisorption, and TPO); Fig. S1 to S12: TPR, XRD patterns,  $CO_2$ -TPD and  $NH_3$ -TPD profiles, reaction mechanisms, HRTEM micrographs, and DRIFT spectra; Table S1: compound selectivities distribution.

## References

- [1] T. J. Schwartz, B. J. O'Neill, B. H. Shanks, J. A. Dumesic, Bridging the Chemical and Biological Catalysis Gap: Challenges and Outlooks for Producing Sustainable Chemicals, *ACS Catal.* 4 (2014) 2060-2069.
- [2] J. I. Di Cosimo, V. K. Díez, C. R. Apesteguía, Base catalysis for the synthesis of  $\alpha,\beta$ -unsaturated ketones from the vapor-phase aldol condensation of acetone, *Appl. Catal., A* 137 (1996) 149-166.
- [3] C. Michel, P. Gallezot, Why Is Ruthenium an Efficient Catalyst for the Aqueous-Phase Hydrogenation of Biosourced Carbonyl Compounds?, *ACS Catal.* 5 (2015) 4130-4132.
- [4] J. Quesada, L. Faba, E. Díaz, S. Bennici, A. Auroux, S. Ordóñez, Role of surface intermediates in the deactivation of Mg-Zr mixed oxides in acetone self-condensation: A combined DRIFT and ex situ characterization approach, *J. Catal.* 329 (2015) 1-9.
- [5] S. Sifniades, A. B. Levy, H. Bahl, in: B. Elvers (Ed.), *Ullmann's Encyclopedia of Industrial Chemistry*, 7th ed., Wiley-VCH Verlag GmbH & Co. KGaA, Weinheim, 2009, Vol. 1, p. 3.
- [6] R. M. West, Z. Y. Liu, M. Peter, C. A. Gärtner, J. A. Dumesic, Carbon-carbon bond formation for biomass-derived furfurals and ketones by aldol condensation in a biphasic system, *J. Mol. Catal., A* 296 (2008) 18-27.
- [7] O. Kikhtyanin, V. Kelbichová, D. Vitvarová, M. Kubů, D. Kubička, Aldol condensation of furfural and acetone on zeolites, *Catal. Today* 227 (2014) 154-162.
- [8] X. Sheng, N. Li, G. Li, W. Wang, A. Wang, Y. Cong, X. Wang, T. Zhang, Direct synthesis of gasoline and diesel range branched alkanes with acetone from lignocellulose, *Green Chem.* 18 (2016) 3707-3711.
- [9] K. A. Goulas, G. Gunbas, P. J. Dietrich, S. Sreekumar, A. M. Grippo, J. P. Chen, A. A. Gokhale, F. D. Toste, ABE Condensation over Monometallic Catalysts: Catalyst Characterization and Kinetics, *ChemCatChem* 9 (2017) 1-10.
- [10] S. Ordóñez, E. Díaz, M. León, L. Faba, Hydrotalcite-derived mixed oxides as catalysts for different C-C bond formation reactions from bioorganic materials, *Catal. Today* 167 (2011) 71-76.
- [11] S. Herrmann, E. Iglesia, Elementary steps in acetone condensation reactions catalyzed by aluminosilicates with diverse void structures, *J. Catal.* 346 (2017) 134-153.
- [12] Z. D. Young, S. Hanspal, R. J. Davis, Aldol Condensation of Acetaldehyde over Titania, Hydroxyapatite, and Magnesia, *ACS Catal.* 6 (2016) 3193-3202.

- [13] L. Faba, E. Díaz, S. Ordóñez, Gas phase acetone self-condensation over unsupported and supported Mg-Zr mixed-oxides catalysts, *Appl. Catal., B* 142-143 (2013) 387-395.
- [14] J. I. Di Cosimo, C. R. Apesteguía, Study of the catalyst deactivation in the base-catalyzed oligomerization of acetone, *J. Mol. Catal., A* 130 (1998) 177-185.
- [15] A. I. Biaglow, J. Sepa, R. I. Gorte, D. A. White, <sup>13</sup>C NMR Study of the Condensation Chemistry of Acetone and Acetaldehyde Adsorbed at the Brønsted Acid Sites in H-ZSM-5, *J. Catal.* 151 (1995) 373-384.
- [16] C. R. Ho, S. Zheng, S. Shylesh, A. T. Bell, The mechanism and kinetics of methyl isobutyl ketone synthesis from acetone over ion-exchanged hydroxyapatite, *J. Catal.* 365 (2018) 174-183.
- [17] A. A. Nikolopoulos, B. W.-L. Jang, J. J. Spivey, Acetone condensation and selective hydrogenation to MIBK on Pd and Pt hydrotalcite-derived Mg-Al mixed oxide catalysts, *Appl. Catal., A* 296 (2005) 128-136.
- [18] M. Balakrishnan, G. E. Arab, O. B. Kunbargi, A. A. Gokhale, A. M. Grippo, F. D. Toste, A. T. Bell, Production of Renewable Lubricants via Self-condensation of Methyl ketones, *Green Chem.* 18 (2016) 3577-3581.
- [19] Z. Xu, L. Wang, X. Wu, Y. Xu, R. Chi, P. Li, J. Zhao, Separation of zirconium and hafnium by solvent extraction using mixture of DIBK and P204, *Hydrometallurgy* 165 (2016) 275-281.
- [20] A. C. C. Rodrigues, J. L. F. Monteiro, Direct synthesis of MIBK from acetone over Pd/NaX catalysts, *Appl. Catal., A* 362 (2009) 185-192.
- [21] Y.-L. Hwang, T. C. Bedard, in: C. Ley (Ed.), *Kirk-Othmer Encyclopedia of Chemical Technology*, John Wiley & Sons, Inc., 2001, Vol. 14 (Ketones), p. 7.
- [22] M. Makosch, W.-I. Lin, V. Bumbálek, J. Sá, J. W. Medlin, K. Hungerbühler, J. A. van Bokhoven, Organic Thiol Modified Pt/TiO<sub>2</sub> Catalysts to Control Chemoselective Hydrogenation of Substituted Nitroarenes, *ACS Catal.* 2 (2012) 2079-2081.
- [23] H. U. Blaser, A. Schnyder, H. Steiner, F. Rössler, P. Baumeister, in: G. Ertl, H. Knözinger, F. Schüth, J. Weitkamp, *Handbook of Heterogeneous Catalysis*, 2nd ed., Wiley-VCH Verlag GmbH & Co. KGaA, Weinheim, 2008, Vol. 7, p. 3286-3288.
- [24] J. I. Di Cosimo, C. R. Apesteguía, M. J. L. Ginés, E. Iglesia, Structural Requirements and Reaction Pathways in Condensation Reactions of Alcohol on Mg<sub>y</sub>AlO<sub>x</sub> Catalysts, *J. Catal.* 190 (2000) 261-275.

- [25] J. Quesada, L. Faba, E. Díaz, S. Ordóñez, Tuning the selectivities of Mg-Al mixed oxides for ethanol upgrading reactions through the presence of transition metals, *Appl. Catal., A* 559 (2018) 167-174.
- [26] K. Cheng, W. Zou, J. Kang, S. He, S. Shi, Q. Zhang, Y. Pan, W. Wen, Y. Wang, Bifunctional Catalysts for One-Step Conversion of Syngas into Aromatics with Excellent Selectivity and Stability, *Chem* 3 (2017) 334-347.
- [27] F. Al-Wadaani, E. F. Kozhevnikova, I. V. Kozhevnikov, Pd supported on Zn<sup>II</sup>-Cr<sup>III</sup> mixed oxide as a catalyst for one-step synthesis of methyl isobutyl ketone, *J. Catal.* 257 (2008) 199-205.
- [28] A. C. C. Rodrigues, J. L. F. Monteiro, C. A. Henriques, Ni-containing mixed oxides as catalysts for the one-step synthesis of methyl-isobutyl-ketone (MIBK) from acetone, *C. R. Chim.* 12 (2009) 1296-1304.
- [29] M. Mediavilla, L. Melo, Y. Díaz, A. Albornoz, A. Llanos, J. L. Brito, MIBK from acetone on Pd/H-[Ga]ZSM5 catalysts: Effect of metal loading, *Microporous Mesoporous Mater.* 116 (2008) 627-632.
- [30] P. P. Yang, J. F. Yu, Z. L. Wang, M. P. Xu, Q. S. Liu, X. W. Yang, T. H. Wu, Preparation, characterization of MCM-56 and catalytic activity in one-step synthesis of MIBK from acetone, *Catal. Commun.* 6 (2005) 107-111.
- [31] S. Herrmann, E. Iglesia, Selective conversion of acetone to isobutene and acetic acid on aluminosilicates: Kinetic coupling between acid-catalyzed and radical-mediated pathways, *J. Catal.* 360 (2018) 66-80.
- [32] R. Unnikrishnan, S. Narayanan, Metal containing layered double hydroxides as efficient catalyst precursors for the selective conversion of acetone, *J. Mol. Catal., A* 144 (1999) 173-179.
- [33] Y. Z. Chen, C. M. Hwang, C. W. Liaw, One-step synthesis of methyl isobutyl ketone from acetone with calcined Mg/Al hydrotalcite-supported palladium or nickel catalysts, *Appl. Catal., A* 169 (1998) 207-214.
- [34] A. N. Mansour, Characterization of NiO by XPS, *Surf. Sci. Spectra* 3 (1994) 231-238.
- [35] L. S. Hsu, R. S. Williams, Electronic-structure study of the Ni-Ga and the Ni-In intermetallic compounds using X-ray photoemission spectroscopy, *J. Phys. Chem. Solids* 55 (1994) 305-312.
- [36] C. E. Dubé, B. Workie, S. P. Kounaves, A. Robbat, M. L. Aksu, Electrodeposition of Metal Alloy and Mixed Oxide Films Using a Single-Precursor Tetranuclear Copper-Nickel Complex, *J. Electrochem. Soc.* 142 (1995) 3357-3365.

- [37] S. O. Saied, J. L. Sullivan, T. Choudhury, C. G. Pearce, A comparison of ion and fast atom beam reduction in TiO<sub>2</sub>, *Vacuum* 38 (1988) 917-922.
- [38] A. R. González-Elípe, G. Munuera, J. P. Espinos, J. M. Sanz, Compositional changes induced by 3.5 keV Ar<sup>+</sup> ion bombardment in Ni-Ti oxide systems: A comparative study, *Surf. Sci.* 220 (1989) 368-380.
- [39] M. Romeo, J. Majerus, P. Legare, N. J. Castellani, D. B. Leroy, Photoemission study of Pt adlayers on Ni(111), *Surf. Sci.* 238 (1990) 163-168.
- [40] C. Hinnen, D. Imbert, J. M. Siffre, P. Marcus, An in situ XPS study of sputter-deposited aluminium thin films on graphite, *Appl. Surf. Sci.* 78 (1994) 219-231.
- [41] J. Z. Shyu, K. Otto, Identification of platinum phases on  $\gamma$ -alumina by XPS, *Appl. Surf. Sci.* 32 (1988) 246-252.
- [42] S. D. Jackson, J. Willis, G. D. McIellan, G. Webb, M. B. T. Keegan, R. B. Moyes, S. Simpson, P. B. Wells, R. Whyman, Supported Metal Catalysts: Preparation, Characterization, and Function: I. Preparation and Physical Characterization of Platinum Catalysts, *J. Catal.* 139 (1993) 191-206.
- [43] T. Huizinga, J. van Grondelle, R. Prins, A temperature programmed reduction study of Pt on Al<sub>2</sub>O<sub>3</sub> and TiO<sub>2</sub>, *Appl. Catal.* 10 (1984) 199-213.
- [44] G. C. Bond, in: M. V. Twigg, M. S. Spencer (Eds.), *Metal-Catalysed Reactions of Hydrocarbons*, Springer, New York, 2005, p. 133-139.
- [45] G. Boskovic, M. Baerns, in: M. Baerns (Ed.), *Basic Principles in Applied Catalysis*, Springer, Heidelberg, 2004, p. 495-496.
- [46] C. Drouilly, J. M. Krafft, F. Averseng, H. Lauron-Pernot, D. Bazer-Bachi, C. Chizallet, V. Lecocq, G. Costentin, Origins of the deactivation process in the conversion of methylbutynol on zinc oxide monitored by operando DRIFTS, *Catal. Today* 205 (2013) 67-75.
- [47] N. E. Fouad, P. Thomasson, H. Knözinger, IR study of adsorption and reaction of methylbutynol on the surface of pure and modified MgO catalysts: probing the catalyst surface basicity, *Appl. Catal., A* 194-195 (2000) 213-225.
- [48] W. F. Wang, A. Stevenson, D. C. Reuter, J. M. Sirota, Absolute band intensities of acetone ((CH<sub>3</sub>)<sub>2</sub>CO) in the infrared region of 830-3200 cm<sup>-1</sup> at low and room temperatures, *Spectrochim. Acta, A* 57 (2001) 1603-1610.
- [49] J. Quesada, L. Faba, E. Díaz, S. Ordóñez, Role of the surface intermediates in the stability of basic mixed oxides as catalysts for ethanol condensation, *Appl. Catal., A* 542 (2017) 271-281.

- [50] A. de Klerk, E. Furimsky, in: J. J. Spivey (Ed.), *Catalysis in the refining of Fisher-Tropsch Syncrude*, RSC Publishing, Cambridge, 2010, RSC Catalysis Series No. 4, p. 136.
- [51] D. Leckel, *Selectivity Effect of Oxygenates in Hydrocracking of Fischer-Tropsch Waxes*, *Energ. Fuel* 21 (2007) 662-667.
- [52] R. P. Young, N. Sheppard, *Infrared Spectroscopic Studies of Adsorption and Catalysis: Acetone and Acetaldehyde on Silica and Silica-Supported Nickel*, *J. Catal.* 7 (1967) 223-233.

### SCHEME CAPTION

**Scheme 1.** Overall proposed mechanism for acetone conversion through combined aldol self-condensation and hydrogenation reactions (DAA: diacetone alcohol; MO: mesityl oxide; MIBK: methyl isobutyl ketone; MIBC: methyl isobutyl carbinol; DIBK: diisobutyl ketone).

### TABLE CAPTION

**Table 1.** Morphological properties and active site distribution and strength of the parent anatase TiO<sub>2</sub> and anatase TiO<sub>2</sub>-based bifunctional catalysts (Pt/TiO<sub>2</sub> and Ni/TiO<sub>2</sub>).

**Table 2.** Acetone conversion and selectivities to main compounds obtained for the first and last measurements (~2 and ~35 ks, respectively) in the acetone self-condensation at 573 K in absence and presence of H<sub>2</sub> (WHSV = 7.9) using anatase TiO<sub>2</sub> and anatase TiO<sub>2</sub>-based bifunctional catalysts (Pt/TiO<sub>2</sub> and Ni/TiO<sub>2</sub>). u-C6 and u-C9 mean unsaturated C6 and unsaturated C9 species, respectively.

### FIGURE CAPTION

**Fig. 1.** Rate of aldol self-condensation of acetone at 573 K in absence of H<sub>2</sub> (WHSV = 7.9). *Dashed lines are meant to guide the eye.*

**Fig. 2.** Selectivity evolution to unsaturated C6 and C9 species with the time-on-stream in the gas-phase self-condensation of acetone at 573 K in absence of H<sub>2</sub> (WHSV = 7.9). *Dashed lines are meant to guide the eye.*

**Fig. 3.** Acetone conversion evolution with the time-on-stream in the gas-phase acetone self-condensation at 573 K in absence and presence of H<sub>2</sub> (WHSV = 7.9). Blue symbols correspond to adjusted values to zero time. The  $k_d$  values are included inside the graphics. *Dashed lines correspond to exponential adjustments as defined in eq. 4.*

**Fig. 4.** Selectivity evolution to: (a) unsaturated C6, and (b) unsaturated C9 species with the time-on-stream in the gas-phase acetone self-condensation at 573 K in presence of H<sub>2</sub> (WHSV = 7.9). *Dashed lines are meant to guide the eye.*

**Fig. 5.** Selectivity evolution to saturated ketones: (a) MIBK, and (b) DIBK with the time-on-stream in the gas-phase acetone self-condensation at 573 K in presence of H<sub>2</sub> (WHSV = 7.9). *Dashed lines are meant to guide the eye.*

**Fig. 6.** Representative HRTEM micrographs of: (a) Pt/TiO<sub>2</sub> (including inside the particle size distribution and the mean size), and (b) Ni/TiO<sub>2</sub>.

**Fig. 7.** Ni/TiO<sub>2</sub> HRTEM images of: (a) a nickel particle, and (b) hybrid crystalline phase of titanium and nickel.

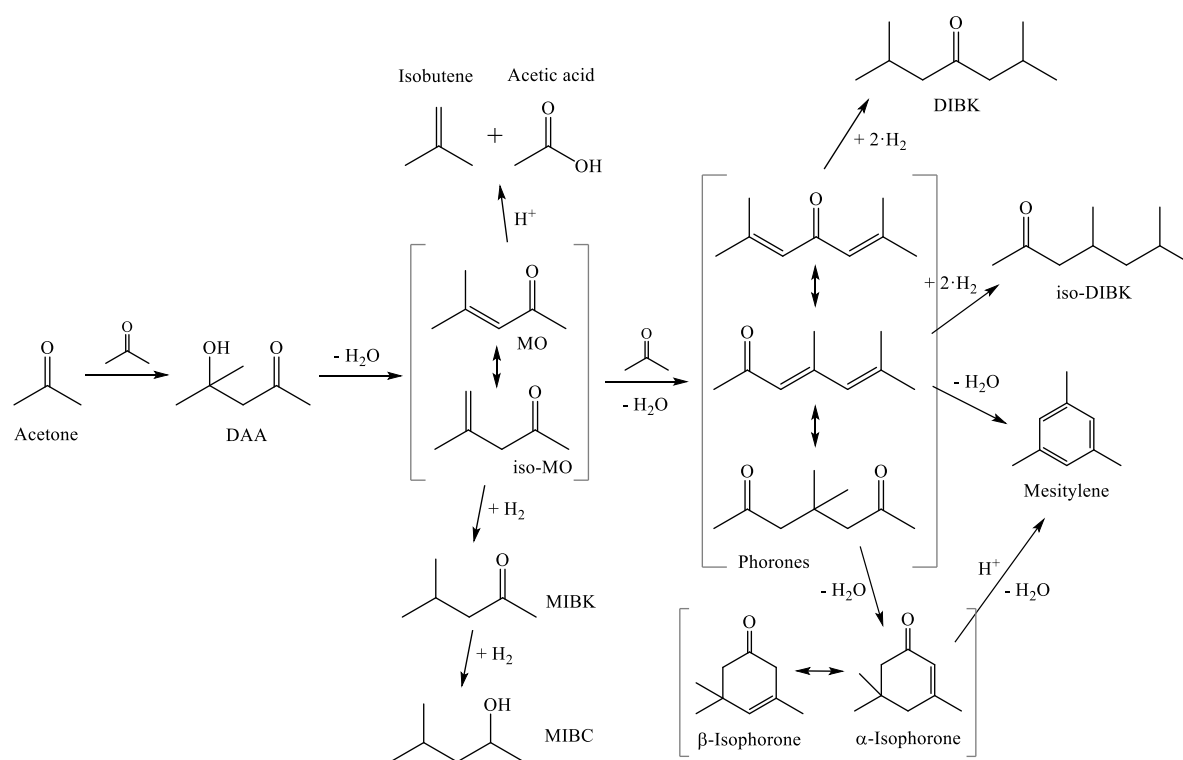
**Fig. 8.** XPS spectra: (a) Ni 2p region of the Ni/TiO<sub>2</sub>, and (b) Pt 4d region of the Pt/TiO<sub>2</sub>. *CPS: counts per second.*

**Fig. 9.** XPS spectra of the Ti 2p region: (a) parent TiO<sub>2</sub>, (b) Ni/TiO<sub>2</sub>, and (c) Pt/TiO<sub>2</sub>. *CPS: counts per second.*

**Fig. 10.** Results obtained by TPO analyses of spent catalysts recovered after 36 ks of time-on-stream in the gas-phase acetone self-condensation at 573 K in absence and presence of H<sub>2</sub> (WHSV = 7.9).

**Fig. 11.** DRIFT spectra recorded during the gas-phase acetone self-condensation at 573 K in presence of H<sub>2</sub> using: (a) TiO<sub>2</sub>, and (b) Pt/TiO<sub>2</sub> and Ni/TiO<sub>2</sub>. *Spectra in part (a) are divided in three*

*differentiated regions multiplied by particular factors, included between brackets, to facilitate the analysis of the absorption bands.*



**Scheme 1.** Overall proposed mechanism for acetone conversion through combined aldol self-condensation and hydrogenation reactions (DAA: diacetone alcohol; MO: mesityl oxide; MIBK: methyl isobutyl ketone; MIBC: methyl isobutyl carbinol; DIBK: diisobutyl ketone).

**Table 1.** Morphological properties and active site distribution and strength of the parent anatase TiO<sub>2</sub> and anatase TiO<sub>2</sub>-based bifunctional catalysts (Pt/TiO<sub>2</sub> and Ni/TiO<sub>2</sub>).

catalyst	S <sub>BET</sub> (m <sup>2</sup> ·g <sup>-1</sup> )	V <sub>p</sub> (cm <sup>3</sup> ·g <sup>-1</sup> )	d <sub>p</sub> (nm)	CO <sub>2</sub> -TPD basic sites (μmol·g <sup>-1</sup> ), [Temperature (K)]			NH <sub>3</sub> -TPD acid sites (μmol·g <sup>-1</sup> ), [Temperature (K)]		
				weak	medium	strong	weak	medium	strong
TiO <sub>2</sub>	50.7	0.57	42.8	1.45, [369]	0.96, [439]	3.55, [657,760]	1.37, [335,375]	1.86, [484,522]	0.21, [690]
Pt/TiO <sub>2</sub>	46.8	0.49	37.0	1.25, [333,363]	0.46, [571]	0.64, [755,787]	1.11, [337,379]	0.93, [450,509]	0.32, [645]
Ni/TiO <sub>2</sub>	44.4	0.46	37.4	2.28, [334,379]	0.04, [624]	0.04, [766]	1.27, [338,379]	1.62, [472,529]	0.33, [670]

**Table 2.** Acetone conversion and selectivities to main compounds obtained for the first and last measurements (~2 and ~35 ks, respectively) in the acetone self-condensation at 573 K in absence and presence of H<sub>2</sub> (WHSV = 7.9) using anatase TiO<sub>2</sub> and anatase TiO<sub>2</sub>-based bifunctional catalysts (Pt/TiO<sub>2</sub> and Ni/TiO<sub>2</sub>). u-C6 and u-C9 mean unsaturated C6 and unsaturated C9 species, respectively.

catalyst	without H <sub>2</sub> , 2 ks / 35 ks			with H <sub>2</sub> , 2 ks / 35 ks					
	x (%)	φ <sub>u-C6</sub> (%)	φ <sub>u-C9</sub> (%)	x (%)	φ <sub>u-C6</sub> (%)	φ <sub>u-C9</sub> (%)	φ <sub>MIBK</sub> (%)	φ <sub>DIBK</sub> (%)	φ <sub>others</sub> (%)
TiO <sub>2</sub>	7.7 / 0.5	69.9 / 100	30.1 / 0	8.0 / 1.0	73.9 / 98.2	26.1 / 1.8	0 / 0	0 / 0	0 / 0
Pt/TiO <sub>2</sub>	7.1 / 0.3	70.3 / 100	29.7 / 0	46.2 / 40.8	0.9 / 1.0	3.1 / 2.4	55.3 / 60.8	36.3 / 34.0	4.4 / 1.8
Ni/TiO <sub>2</sub>	10.9 / 0.1	68.9 / 100	31.1 / 0	14.2 / 10.9	59.2 / 59.1	39.5 / 39.4	1.0 / 1.3	0 / 0	0.3 / 0.2

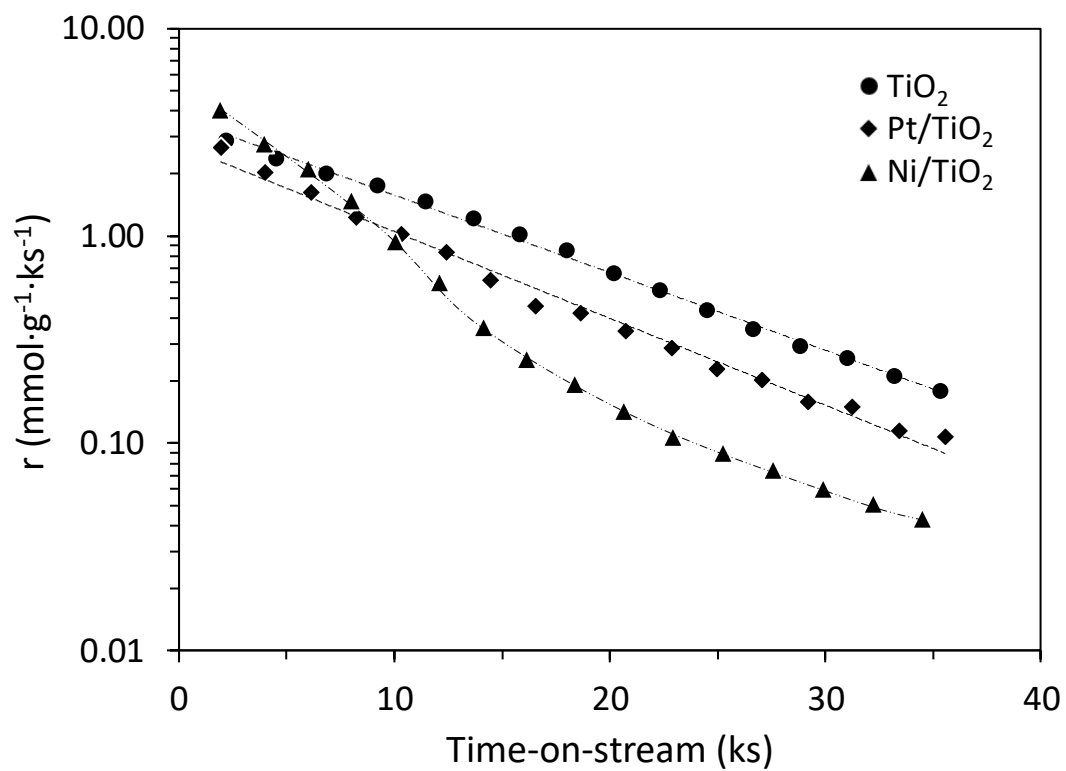


**Fig. 1.** Rate of aldol self-condensation of acetone at 573 K in absence of H<sub>2</sub> (WHSV = 7.9). Dashed lines are meant to guide the eye.

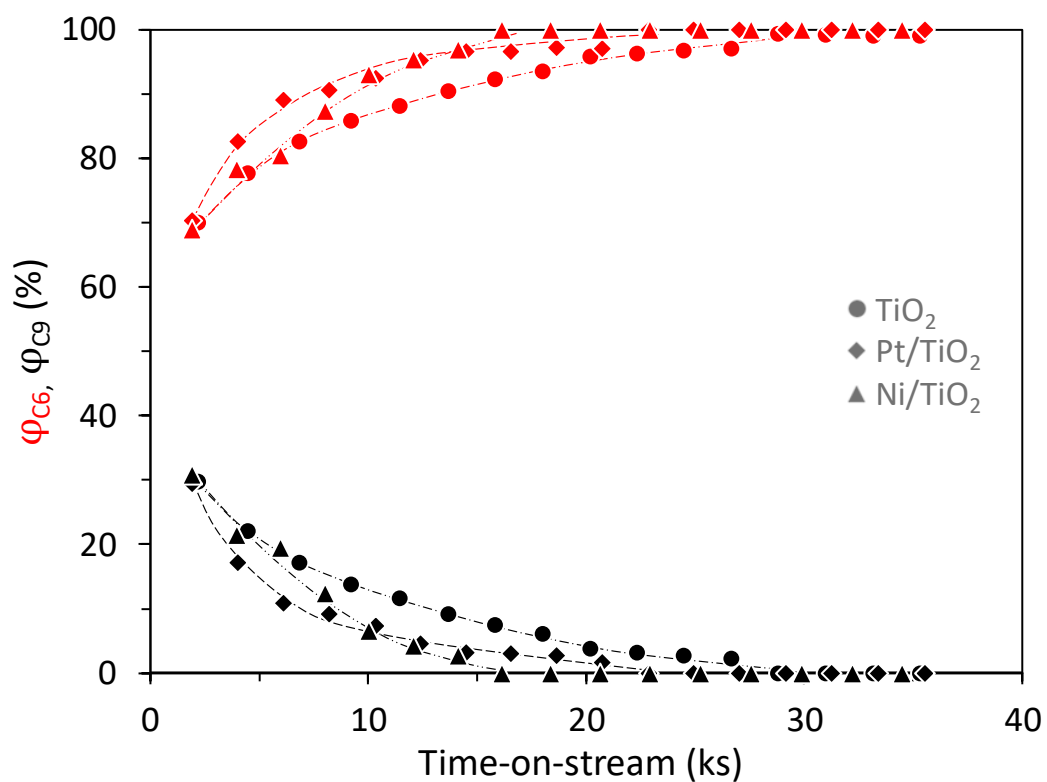


**Fig. 2.** Selectivity evolution to unsaturated C6 and C9 species with the time-on-stream in the gas-phase self-condensation of acetone at 573 K in absence of H<sub>2</sub> (WHSV = 7.9). Dashed lines are meant to guide the eye.

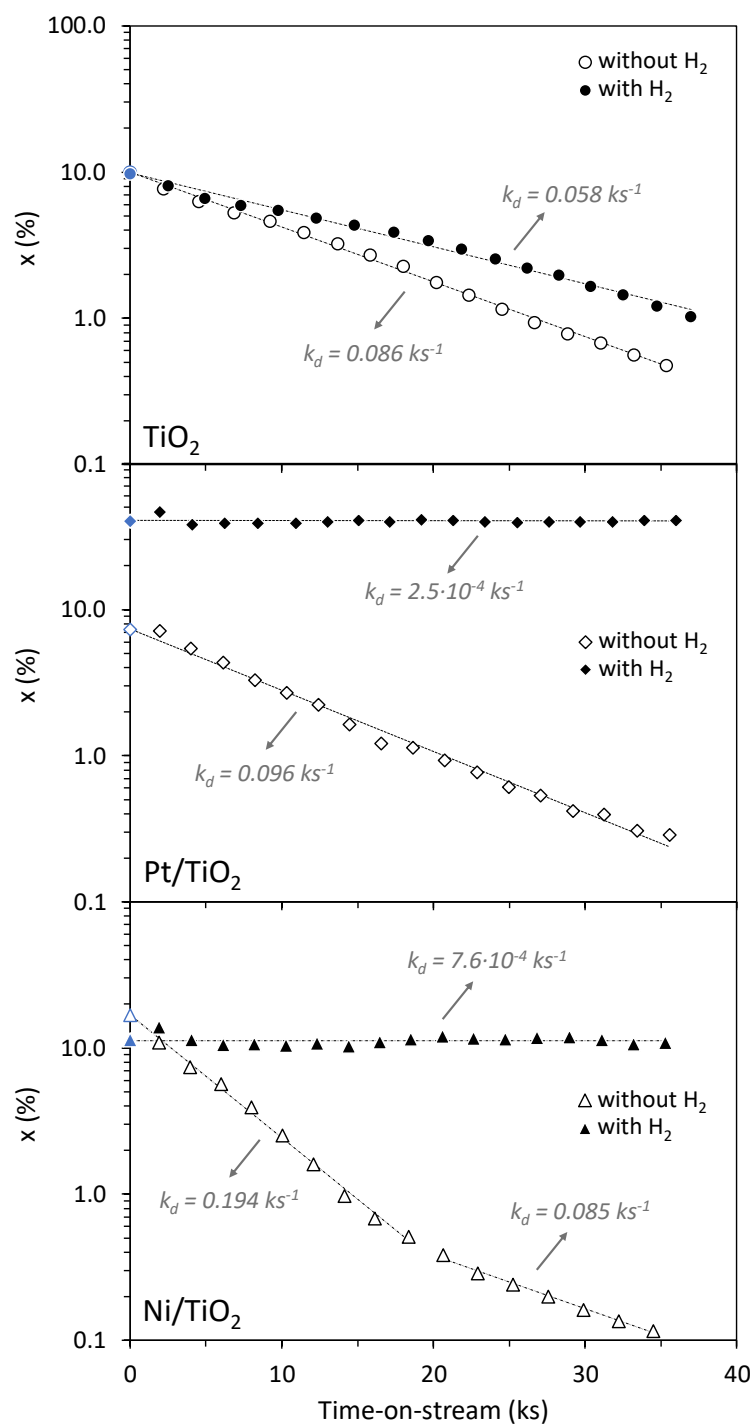


**Fig. 3.** Acetone conversion evolution with the time-on-stream in the gas-phase acetone self-condensation at 573 K in absence and presence of  $\text{H}_2$  (WHSV = 7.9). Blue symbols correspond to adjusted values to zero time. The  $k_d$  values are included inside the graphics. Dashed lines correspond to exponential fits as defined in eq. 4.

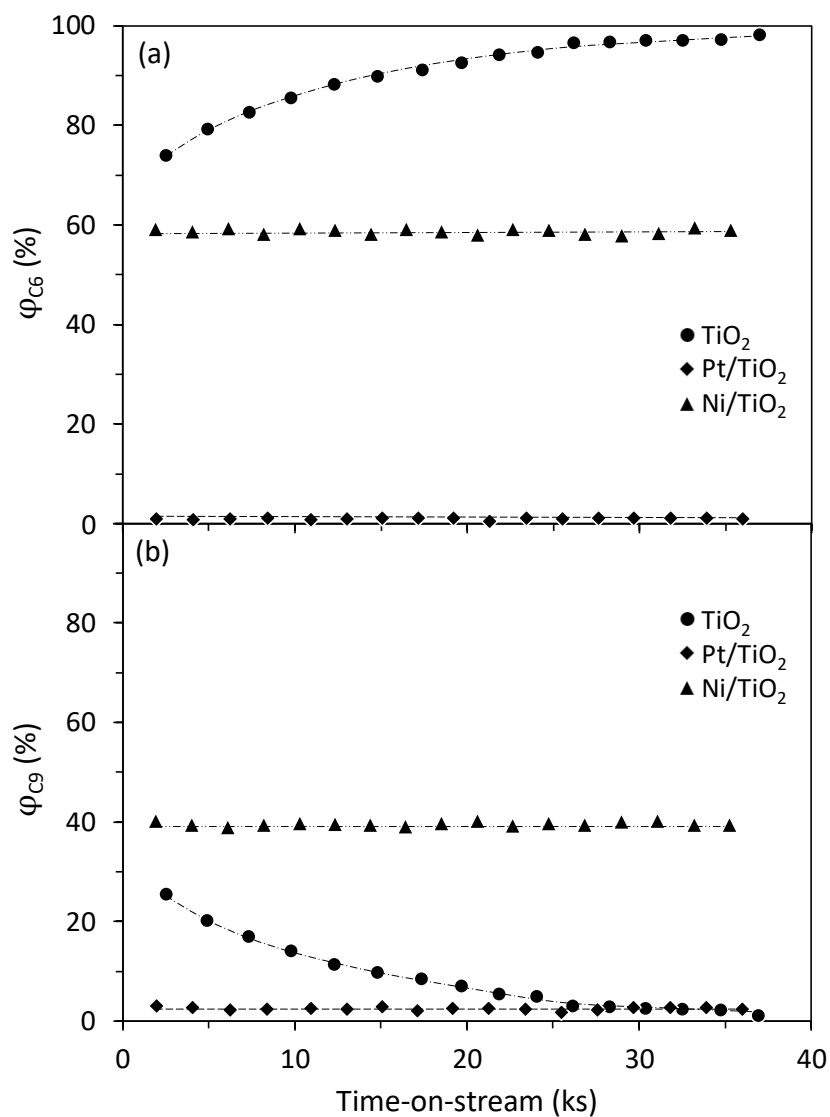


**Fig. 4.** Selectivity evolution to: (a) unsaturated C6, and (b) unsaturated C9 species with the time-on-stream in the gas-phase acetone self-condensation at 573 K in presence of H<sub>2</sub> (WHSV = 7.9). *Dashed lines are meant to guide the eye.*

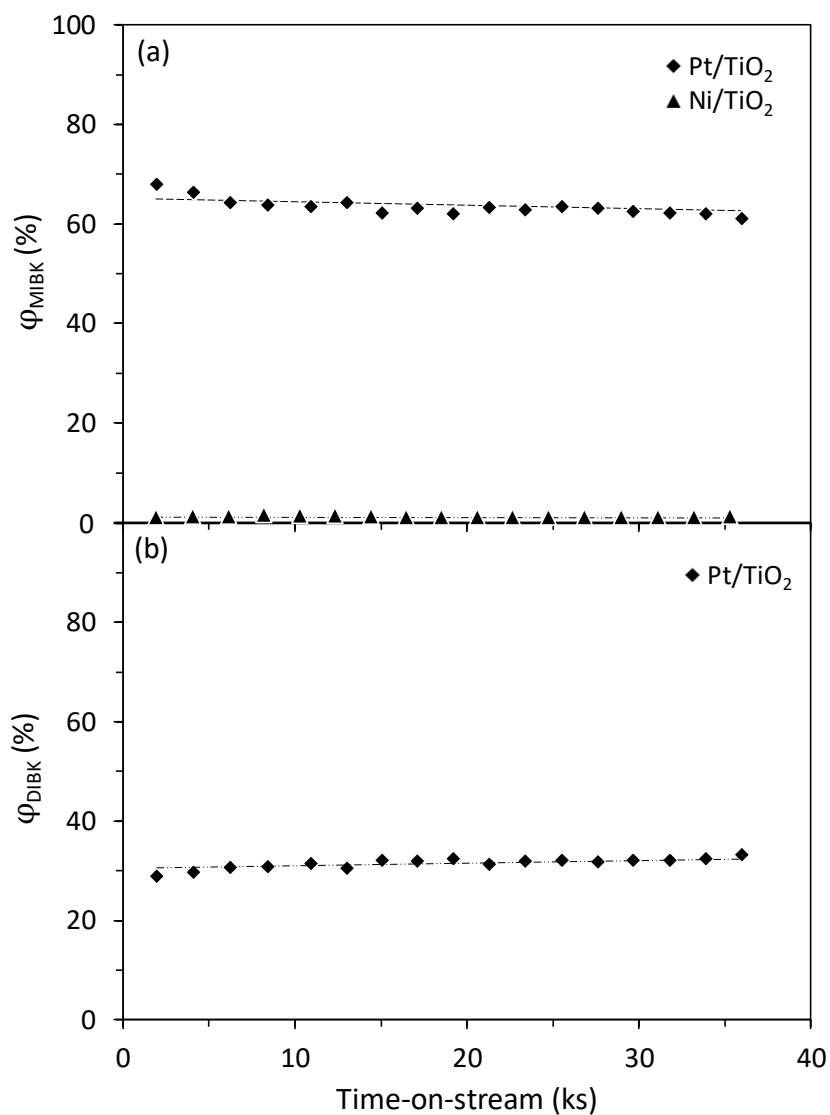


**Fig. 5.** Selectivity evolution to saturated ketones: (a) MIBK, and (b) DIBK with the time-on-stream in the gas-phase acetone self-condensation at 573 K in presence of H<sub>2</sub> (WHSV = 7.9). *Dashed lines are meant to guide the eye.*

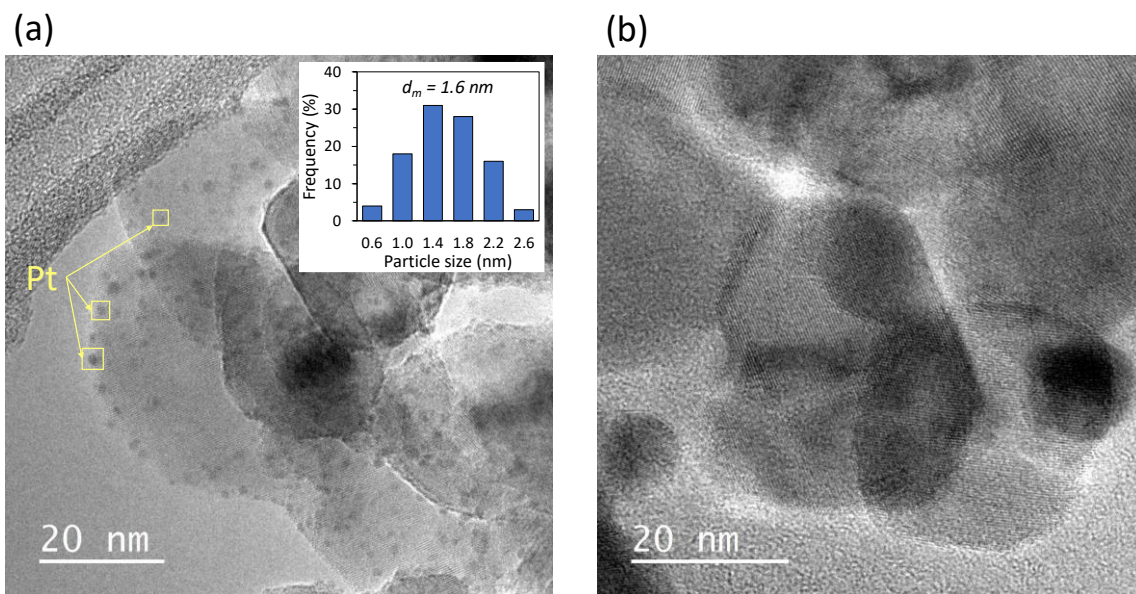


**Fig. 6.** Representative HRTEM micrographs of: (a) Pt/TiO<sub>2</sub> (including inside the particle size distribution and the mean size), and (b) Ni/TiO<sub>2</sub>.

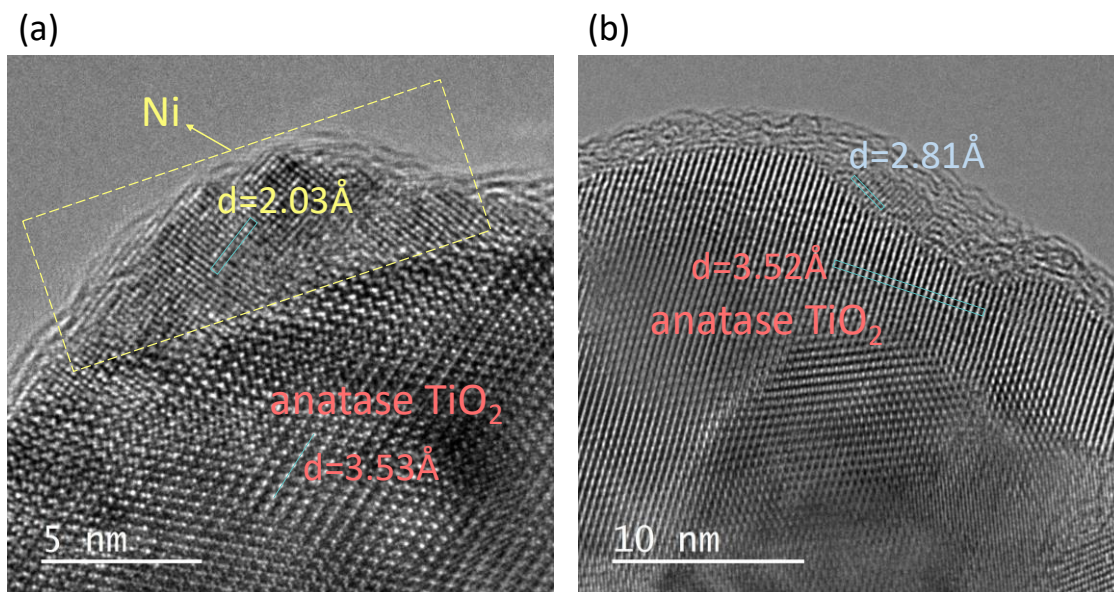


**Fig. 7.** Ni/TiO<sub>2</sub> HRTEM images of: (a) a nickel particle, and (b) hybrid crystalline phase of titanium and nickel.

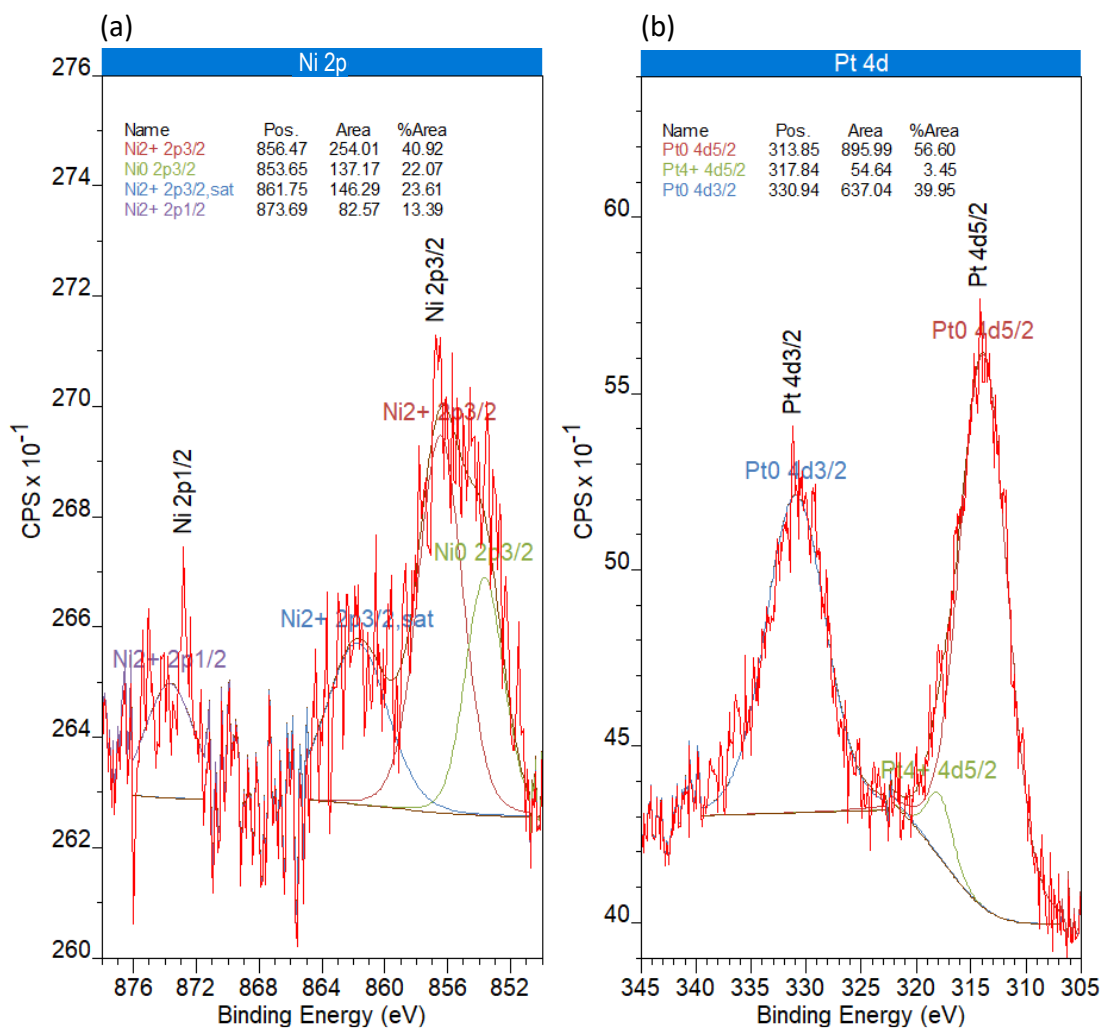


**Fig. 8.** XPS spectra: (a) Ni 2p region of the Ni/TiO<sub>2</sub>, and (b) Pt 4d region of the Pt/TiO<sub>2</sub>. CPS: counts per second.

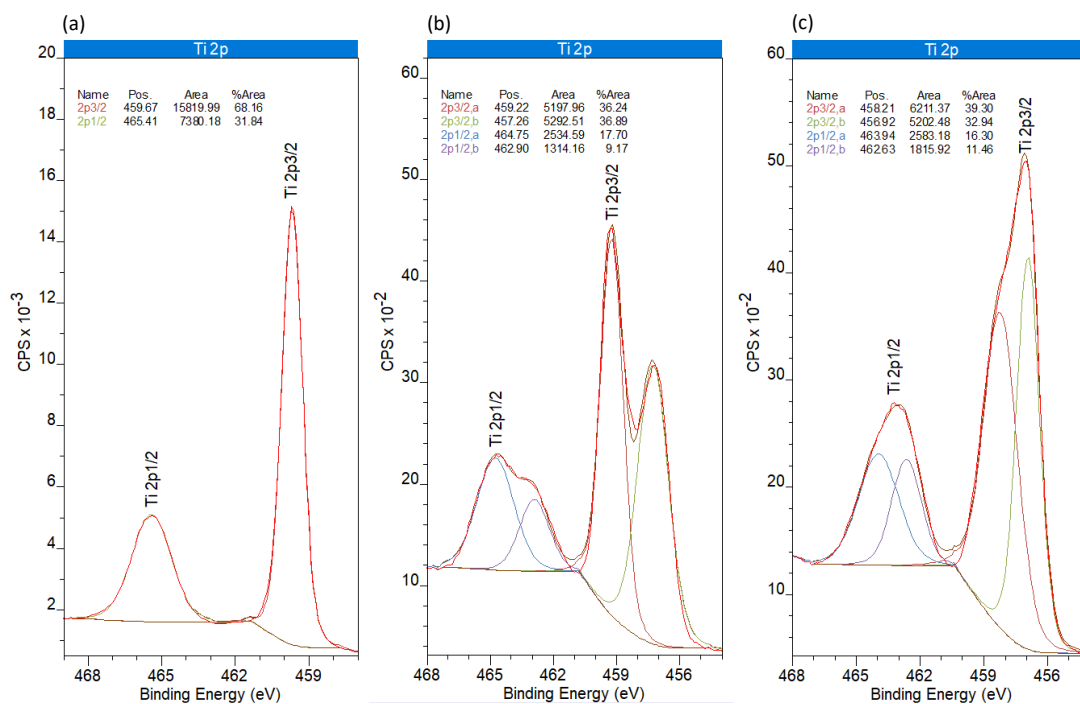


**Fig. 9.** XPS spectra of the Ti 2p region: (a) parent TiO<sub>2</sub>, (b) Ni/TiO<sub>2</sub>, and (c) Pt/TiO<sub>2</sub>.

*CPS: counts per second.*

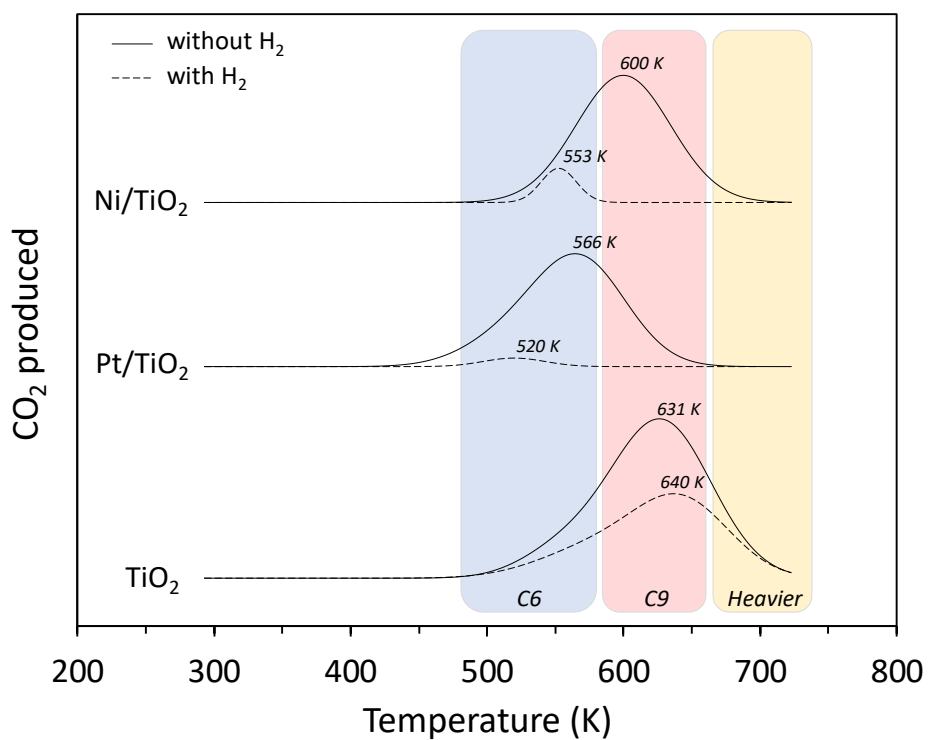


**Fig. 10.** Results obtained by TPO analyses of spent catalysts recovered after 36 ks of time-on-stream in the gas-phase acetone self-condensation at 573 K in absence and presence of H<sub>2</sub> (WHSV = 7.9).

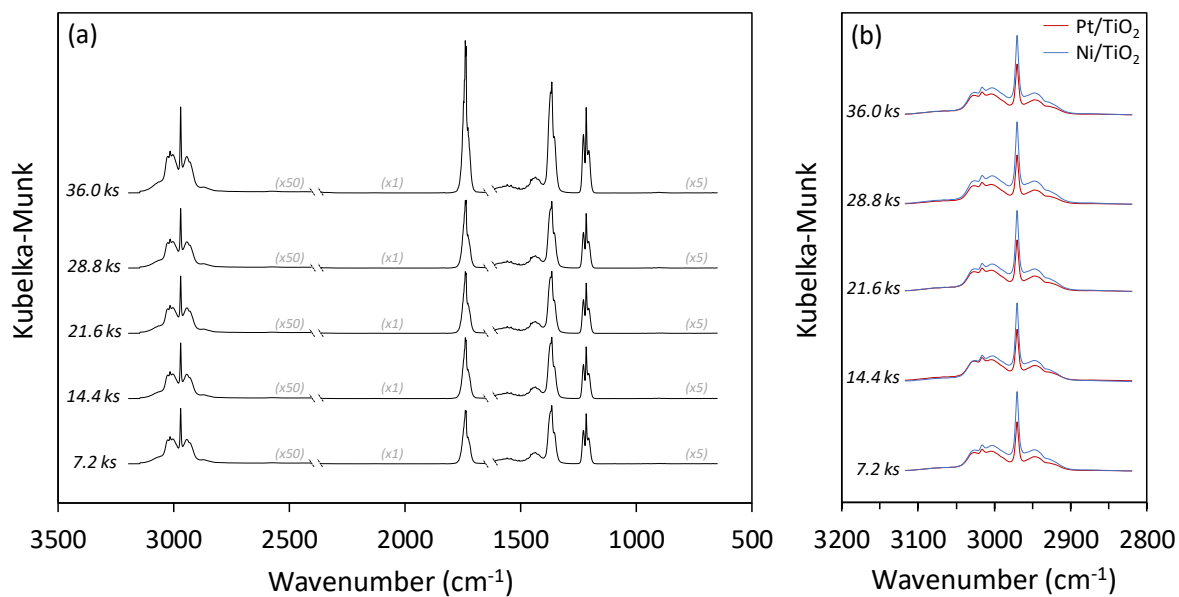


**Fig. 11.** DRIFT spectra recorded during the gas-phase acetone self-condensation at 573 K in presence of  $H_2$  using: (a)  $TiO_2$ , and (b)  $Pt/TiO_2$  and  $Ni/TiO_2$ . Spectra in part (a) are divided in three differentiated regions multiplied by particular factors, included between brackets, to facilitate the analysis of the absorption bands.